Parcellation of Human Inferior Parietal Lobule Based on Diffusion MRI and Resting State Functional MRI

Zhiqian Gui

A dissertation

submitted in partial fulfillment of the

requirements for the degree of

Doctor of Philosophy

University of Washington

2014

Reading Committee:

Linda Shapiro, Chair

Thomas Grabowski

Tara Madhyastha

Program Authorized to Offer Degree:
Department of Electrical Engineering

University of Washington

ABSTRACT

Parcellation of Human Inferior Parietal Lobule Based on Diffusion MRI and Resting State Functional MRI

Zhiqian Gui

Chair of the Supervisory Committee:

Professor Linda G. Shapiro

Electrical Engineering

This thesis describes the parcellation of the human inferior parietal lobule (IPL) based on diffusion MRI and resting state functional MRI. It also describes the in-depth analysis of the dynamic functional networks associated with different areas of the IPL and how to use the dynamic functional networks to parcellate IPL voxels. Although the IPL voxel parcellation was not successful, we made some novel discoveries about voxel-level functional behavior patterns.

TABLE OF CONTENTS

GLOSSARY

BEDPOST – Bayesian estimation of diffusion parameters obtained using sampling techniques

BOLD – blood oxygen level dependent

CBCP – connectivity based cortical parcellation

CSF – cerebrospinal fluid

CWT – continuous wavelet transform

DB – Davies Bouldin

dMRI – diffusion magnetic resonance imaging

EM – Expectation Maximization

fMRI – functional magnetic resonance imaging

ICA – Independent component analysis

IPL – Inferior Parietal Lobule

LR – lexical retrieval

MRI – magnetic resonance imaging

ROI – region of interest

SIL – Silhouette

SLS – Seattle longitudinal study

STFT – short time Fourier transform

TE – time echo

TFE – turbo-field echo

TI – inversion time

TR – repeat time

WTC – wavelet transform coherence

ACKNOWLEDGEMENTS

Completing my Ph.D. research is probably the most intellectually challenging activity of the first 28 years of my life. It was not an easy journey and I was supported by many people during the journey.

My first debt of gratitude must go to my advisor Dr. Linda Shapiro. She gave me some key instructions of the direction of this research. Also she had been working hard to provide me financial assistance throughout my doctoral program.

I am greatly indebted of Dr. Tara Madhyastha who helped me tremendously. The research is very interdisciplinary and the neuroscience part of this project is much more complicated than I expected. Without her patient instructions, I was not able to quickly understand all the key concepts related. Whenever my research was in trouble, she always encouraged me and gave me important ideas. In the process of thesis writing, she revised all my drafts.

I want to express deep gratitude to Dr. Thomas Grabowski. He helped me understand the big picture of the research a lot and provided key insights during critical moments of the research. Without his guidance, I may not be able to know how my work is related to the bigger picture of neuroscience study.

Special thanks to my supervisory committee member Dr. Jenq-Neng Hwang who attended my doctoral defense and gave me good suggestions. Also I am very thankful to my Graduate School Representative Dr. Anshu Narang-Siddarth who attended my doctoral defense.

I wish to thank my parents, Ming Gui and Xuening Ying. Their love provided my inspiration and was my driving force.

Chapter 1 INTRODUCTION

The cerebral cortex is a layer of grey matter, the cell bodies of neurons, approximately 1-4 mm thick, which plays an instrumental role in human cognitive activities. A cortical field is a cluster of cells in a circumscribed region of the cerebral cortex that executes a specific function. The act of parcellation of the cortex is dividing the cortex into different anatomical or functional parcels. Anatomical parcels may be delineated using anatomical boundaries, but functional parcels are harder to circumscribe. Parcellation is difficult, because people vary in their neuroanatomy, meaning that corresponding cortical fields will be different shapes and sizes and in slightly different locations. Therefore, although atlases exist that are based on group averages and indicate where specific cortical regions are expected to be, they do not match any one individual. Parcellation of the cortex is an important problem because different regions of the brain perform different functions. Furthermore, different regions of the brain are involved in different networks that together act to produce higher order cognition. Therefore, obtaining a functional parcellation of these regions allows researchers to examine the properties of functional cortical regions that are involved in specific functions and networks. For example, such properties may be structural connectivity, a measure of how tightly connected one region is with another via white matter fibers, or functional connectivity – how a region functions similarly to another region.

The Inferior Parietal Lobule (IPL) is a cortical area that is a particularly interesting testbed for development of parcellation methods, because it is involved in multiple brain networks (default network, visual network, language network, etc). Moreover, it has a complicated cytoarchitectural structure (the arrangement and characteristic organization of neuronal cell bodies), with multiple diverse cortical fields in a relatively small area of the cortex (that has been well studied). If we have a reasonable tool to parcellate the IPL for an individual subject, this would allow us to measure aspects of the role of the IPL in specific networks more accurately. For example, one could test the hypothesis that a cortical field may

be involved in only one function at a time. One could examine individual differences in cortical field properties (e.g. volume, thickness, or connectivity) that might relate to behavior. In this thesis, we will discuss background material and related research in Chapter 2. We will describe the data acquisition parameters and preprocessing pipelines in Chapter 3. We will describe dMRI and fMRI based clustering methods in Chapter 4. We will discuss the dynamic analysis, machine learning based parcellation method and multiple cluster analysis in Chapter 5. We will conclude in Chapter 6.

Chapter 2 BACKGROUND AND RELATED RESEARCH

This dissertation is highly interdisciplinary, integrating neuroimaging, neuroscience, machine learning and signal processing. This chapter provides an overview of the methods and research that lay the foundation for this project. Magnetic resonance imaging methods (diffusion magnetic resonance imaging (dMRI) and functional magnetic resonance imaging (fMRI)) that provide in vivo structural and functional information about individual connectivity are enabling technologies, described in Section 2.1. The focus of this research is the IPL, an anatomical region with a complex function and unique individual anatomical variability, described in Section 2.2. Individual differences in the organization of cortical regions can only be determined in vivo using a parcellation technique. Parcellation methods based on dMRI and fMRI, with applications to the IPL, are described in Section 2.3. Finally, a key insight is that time-varying correlations between fMRI timecourses of functionally connected regions may provide additional information to enhance traditional fMRI and dMRI cortical parcellation methods. We describe work related to dynamic connectivity and introduce appropriate time-frequency methods of analysis in Section 2.4.

2.1 Magnetic Resonance Imaging Methods

In this section we describe the magnetic imaging resonance technologies and associated analyses techniques that allow us to examine the connectivity of the IPL to the rest of the cortex. Section 2.1.1 describes dMRI and probabilistic tractography, an analysis technique used to reconstruct fiber pathways from one cortical region to another. Section 2.1.2 describes resting state fMRI.

2.1.1 An Overview of dMRI and Probabilistic Tractography

dMRI is a technique that allows quantification of the movement of water in the brain. Because water moves in axons, the structural properties of axons constrain diffusion of water. Using this property, we

can estimate the strength of fiber tracts connecting one voxel to another. Probabilistic tractography calculates the probability that a seed voxel is connected to a target region.

2.1.1.1 Diffusion MRI Model

Diffusion imaging is an MR method that produces images with strong contrast of molecular diffusion, generally water[1]. In some tissues, such as white matter in the brain or muscle fibers in the heart, water molecules diffuse heterogeneously in different directions. The diffusion tensor model assumes that the movements of particles follow a simple anisotropic diffusion process in which the diffusion tensor is a zero-mean Gaussian distribution [2], [3]. Multiple acquisitions with different orientations of the diffusion sensitizing gradients are conducted to compute the diffusion tensors of each voxel. However, this model can only work well in voxels containing fibers that are aligned in a single direction and does not accurately model voxels with crossing fibers (which is the norm) due to its mathematical oversimplification. To overcome such limitations, we employ a partial volume model in which the diffusion property of each voxel is modeled as the summation of a number of anisotropic components and one isotropic component. The model is fit using a Markov Chain Monte Carlo sampling technique that estimates the posterior distribution of parameters in the model. This method is called Bayesian Estimation of Diffusion Parameters Obtained using Sampling Techniques (BEDPOST) [4].

2.1.1.2 Probabilistic Tractography

In this project, we are interested in quantifying white matter connectivity, because different brain regions communicate through white matter. We use a probabilistic tractography technique to obtain a measurement of the strength of connectivity between different cortical regions. In the probabilistic method, the propagation of molecules at each voxel follows different fiber orientations with different probabilities. A Monte Carlo method is used to simulate the particle propagation process from a seed voxel to a target region for 5000 times and count the probability of a particle arriving one target region from another seed voxel [4]. In our study, the target regions are parcels from the Destrieux atlas [5],

quantified by Freesurfer[6], a set of tools for analysis and visualization of structural and functional brain imaging data. Seed regions are voxels 2mm underneath the white/grey matter interface that belong to either the left angular gyrus or the left supramarginal gyrus, or the left Jensen sulcus. Here, Destrieux parcels are obtained from the technique that automatically assigns a neuroanatomical label to each location on a cortical surface model based on probabilistic information estimated from a manually labeled training set [7]. By tracking the connectivity from each seed to all targets, we calculate the connection matrix indicating probabilistic connections between each IPL voxel and each non-IPL Region of Interest (ROI).

2.1.2 An Overview of Resting State fMRI

In neuroimaging research, fMRI is widely used as a non-invasive technique to quantify neuronal activation. Because blood oxygenation and flow change in response to neural activity, the changes in the blood-oxygen-level-dependent (BOLD) signal can be measured when the subject is performing a task. Brain areas with BOLD change that is correlated with the task are identified as areas of activation. However, the BOLD signal of a person collected while at rest (not engaged in a task) also conveys important information about brain networks. Recent studies report that large scale brain networks are not idle during rest, but display a rich amount of spontaneous activity that reveal large scale brain network structures [8]. The strength of the correlation between cortical regions is thought to reflect the strength of the functional connection between the regions. Strongly functionally connected regions at rest are called resting-state networks.

Approximately eight functionally connected networks have been identified robustly in different samples of individuals. They are the primary motor network, primary visual network, extra-striate visual network, insular-temporal network, left parietal-frontal network, right parietal-frontal network, default mode network and frontal network, as shown in Figure 1[9]. Among those major networks, the default mode network behaves quite differently because the default mode network shows an elevated level of neuronal

activation during rest than performing tasks. This finding suggests that this network acts like a default state of the human brain [10]. The activities of the default mode network are related to internally focused tasks including autobiographical memory retrieval, envisioning the future, and conceiving the perspectives of others, so the default mode network is of special research interest [10].

The IPL is an interesting region to study because the PGp (a part of IPL that will be described in section 2.2) is involved in the default mode network and the other parts of the IPL are not. In our study of IPL parcellation, we use resting-state fMRI instead of task-based fMRI data, because only resting-state functional data enables whole brain analysis and a resting-state scan is much easier and cheaper to conduct than a task-based scan.

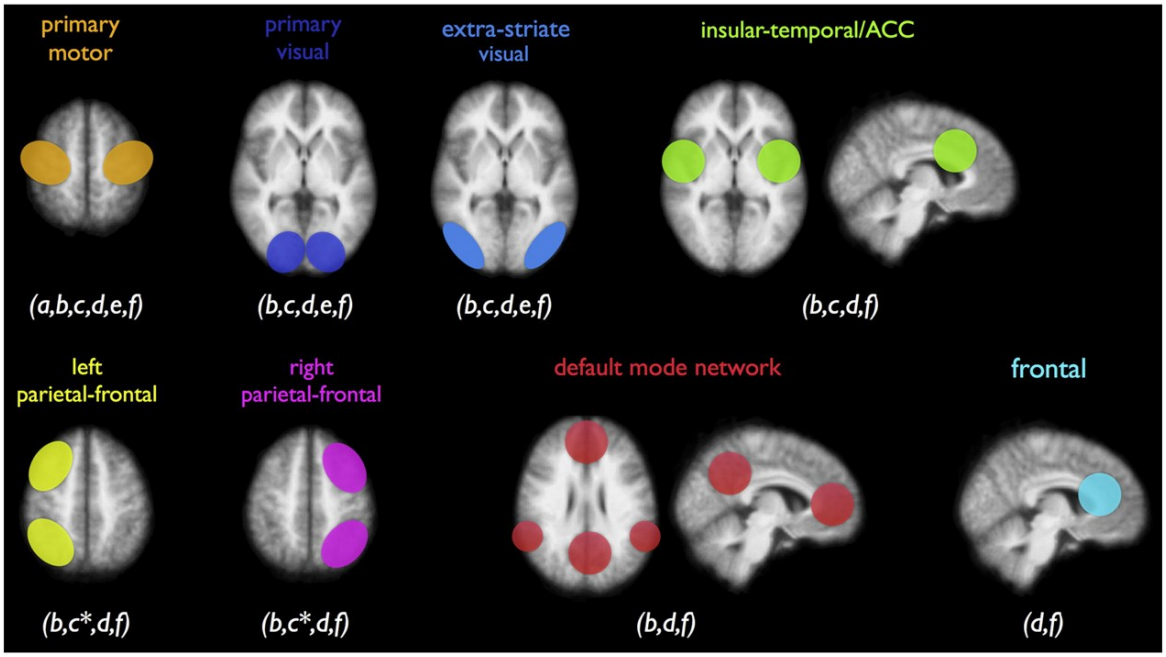

Figure 1 Resting state functional networks [9]

2.2 The Inferior Parietal Lobule

The inferior parietal lobule is an area of cortex in the parietal lobe that integrates various modalities (e.g., somatosensory, visual, and auditory) and plays an important role in various higher cognitive functions. We are very interested to know if this functional complexity is reflected at a structural level [11]. In the study of Caspers et al, the probabilistic and observer-independent procedures were applied to analyze 10

postmortem brains (5 male and 5 female) for the cytoarchitectonic (the packing density and laminar distribution of pyramidal and non-pyramidal neurons) organization of the IPL [11]. A mosaic of seven areas was found. Five areas PF, PFcm, PFm, PFop and PFt, are located on the supramarginal gyrus and two areas, PGa and PGp, lie on the angular gyrus [11]. The names are adopted from nomenclature of Von Economo and Koskinas [12]. In our parcellation study, we are especially interested in differentiating between the PGa and PGp, because the PGp is involved in the default mode network while PGa is not [13]. Different parts of the IPL are illustrated in Figure 2. Compared to other regions of the cortex, functional and diffusion tensor imaging of the IPL is much less affected by artifacts, so the IPL is a good region to start our investigation of cortical parcellation methods using functional and diffusion tensor imaging.

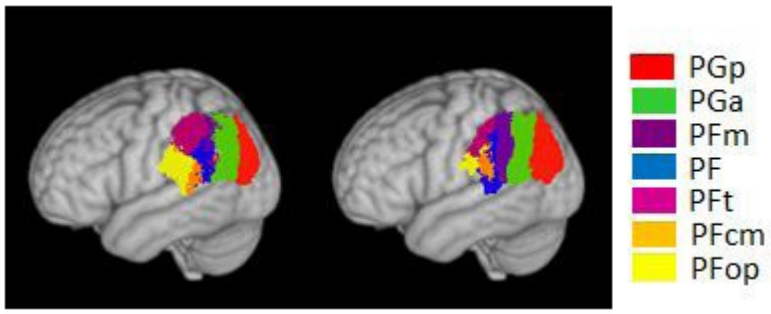

Figure 2 IPL Anatomy [14]

2.3 Parcellation of the Cortex

The purpose of parcellation of the cortex is to cluster similar cortical areas based on some criteria, such as cytoarchitectural similarity (microstructural features of laminar thickness, cell size, packing density) [14], structural connectivity and functional connectivity. In the human brain, higher order functions are the product of coordinated activity among cortical regions specialized for specific activity. Neural activity in different regions comprising large scale brain networks tends to be correlated over time. Therefore, in order to understand the functional organization of brain networks, it is important to identify regions that have distinct functions.

A simple approach to the parcellation problem is to use an Atlas or a map of regions in standard space that has been created from the average of a group of human brains. For example, the Jüliech atlas[11] is an atlas derived from cytoarchitectural (cellular) data. However, the specific boundaries of cortical regions for different individuals vary quite a lot, so an atlas-based approach is not ideal. Any specific individual may or may not be well aligned with the atlas. Unfortunately, there is no way to obtain cytoarchitectural data from a living person, so we must rely upon noninvasive (but approximate) techniques based on MRI to parcellate the cortex of a living individual. The hypothesis that the functional organization of the human cerebral cortex is based on functional fields each occupying a specific, relatively large territory of the cortex [15] motivates the use of dMRI, fMRI and their combination for parcellation. Using dMRI and fMRI, we are able to have subject specific and in vivo parcellations.

Section 2.3.1 describes clustering algorithms (and evaluation of these algorithms) that can be used to cluster similar cortical areas. Section 2.3.2 describes approaches to parcellation using dMRI, and section 2.3.3 describes approaches to parcellation using fMRI.

2.3.1 Clustering Algorithms and Evaluation

Data clustering is the unsupervised classification of patterns into distinct groups. The clustering problem has been extensively studied in many contexts and many disciplines, and multiple different methods have been developed for data clustering. K-means, sparse K-means, Expectation–Maximization (EM), mean-shift, spectral clustering, region growing and normalized graph cuts are among the most popular algorithms in computer vision. The K-means algorithm aims to partition observations into clusters in which each observation belongs to the cluster with the nearest mean [16]. The EM algorithm tries to find the closest distribution (usually a Gaussian mixture model) to fit the data. It starts from initial guesses of mean, variance and weight of each data clusters and then updates them iteratively [17]. Normalized graph cuts is a spectral clustering algorithm which represents the feature space as a graph [18]. It partitions the

vertices of the graph into two sets based on the eigenvector, corresponding to the second-smallest eigenvalue of the generalized eigenvalue problem. In the study of the cortical parcellation problem, we employed the EM algorithm.

In this parcellation project, there is no 'ground truth' for each subject, because the Jüliech Atlas is the average parcellation of 10 post-mortem brains. The closest available parcellation to the ground truth is the registration of the Jüliech Atlas labels from NMI space to subject-specific spaces. We have developed several methods for comparing parcellations based on data clustering and parcellations based on the Jüliech Atlas. Soran et al. [19] developed a metric to evaluate the degree of overlap between different parcellations, and parcellations with more overlap with the Atlas are considered better. We used several internal metrics [20] to evaluate within-cluster similarity versus cross-cluster similarity. The parcellation is considered good if within-cluster similarity is small comparing to cross-cluster similarity.

2.3.2 Parcellation Based on dMRI

A number of studies have started to cluster gray matter structures including thalamus and cerebral cortex based on analysis of dMRI data. This approach is known as connectivity-based cortical parcellation (CBCP) [14]. The basic premise for CBCP is that spatially adjacent voxels with similar long range structural connectivity patterns are also cytoarchitectonically similar [12]. This enables a non-invasive method of cortical parcellation. The dMRI based on probabilistic tractographic method had been used for the connectivity based parcellation of Broca's area [21]. It was also used to differentiate between pre-SMA and SMA and between area 44 and area 45[22]. DMRI tractography was used to segregate the lateral premotor cortex dorsal(PMd) and later Premotor cortex ventral (PMv) parts based on their distinctive patterns of connectivity with frontal cortex and lateral parietal cortex [23]. The human lateral parietal cortex was parcellated into component regions on the basis of anatomical connectivity (estimated by dMRI tractography) and functional connectivity(estimated by resting state fMRI) with other brain regions [24]. A dMRI tractography technique was applied to parcellate the corpus callosum (CC) into six

major subdivisions based on trajectories to different cortical areas. They found significant atrophy in the motor and sensory areas of patient CC in comparison to normal CC[25]. The amygdala area was subdivided by applying spectral clustering algorithm to cluster principle diffusion direction in each voxel. A consistent subdivision of amygdala into a medial and a lateral region was found in good agreement with fiber architecture in post-mortem human brain[26]. The parcellation of the cortical surface was studied based on the connectivity of each vertex to 36 large gyri. The K means algorithm with spatial regularization was used[27]. Probabilistic connectivity between cingulate cortex and 11 predefined target ROIs were calculated to parcellate the cortex. Functional studies were conducted to confirm that regional functional specialization was found to be related to the parcels clustered based on probabilistic connectivity [28].

In the work of Soran et al, IPL voxels are clustered based on the connection matrix resulted from dMRI probability tractography pipeline mentioned in section 2.1.1.2. The feature vector for each voxel is the probabilistic connection between it and all target ROIs combined with Euclidean coordinates of IPL voxels. Using the normalized graph cut algorithm, she achieved an average of 64% overlap with the Jüliech Atlas[19]. In our work, we didn't consider the spatial coordinates of IPL voxels, because we thought Euclidean distance is not a good measure of spatial affinity on cortical structure. We used the EM algorithm for clustering feature vectors. The clusters were initialized by the clusters resulting from registering the atlas to individual specific space.

2.3.3 Parcellation Based on fMRI

If anatomically similar regions have similar functional activation, fMRI can provide important clues for parcellation. Voxels of a cortex are parcellated into different sub regions based on the similarity of their functional time courses. This method was used to parcellate the medial frontal cortex (MFC) into supplementary motor areas (SMA) and pre-SMA subregions[29] and to parcellate the visual cortex and intraparietal sulcus [30]. Parcellation of the Posterior Parietal Cortex according to the fMRI based on

orientation discrimination tasks of real rotating and mentally rotating alpha-numeric characters was studied by Katherine et al [31]. In the work of Jane et al [32] replicator dynamics was used as an exploratory analysis tool to detect sub regions of left lateral frontal cortex on the basis of the similarity between fMRI time series. In the work of Karkar et al, a hierarchical clustering algorithm was developed to parcellate brain regions [33]. Functional specialization for different aspects of cue processing in the lateral and medial subregions of the frontal and parietal cortex was found [34]. Normalized graph cuts with spatial constraints was applied to produce smooth parcellation of medial superior frontal cortex[35]. A novel approach combining anatomical and functional information was used by Saclay et al to parcellate the whole brain [36]. Friman et al. used canonical correlation analysis, a multivariate extension of univariate correlation analysis to detect homogeneous regions of activity [37].

2.4 Dynamic Functional Connectivity and Time-Frequency Analysis

Recent studies show that resting-state functional connectivity is not static and that RSNs can exhibit nonstationary, spontaneous relationships irrespective of conscious, cognitive processing [38]. Researchers have demonstrated that the mean correlations in the brain vary dynamically through time [39]. Wavelet coherence based time frequency analysis reveals scale-dependent temporal variability across resting state network[39]. High degree of variability of resting state network activities was observed by Jones et al. They also tested that such variability is not simply resulted from noise but further indicates the non-stationary nature of brain functional network [40]. In the study of functional networks, current correlation-based approaches measure the average functional connectivity between regions, but this method falls short in analyzing regions that are involved in multiple networks. Smith et al took advantage of the temporal variation to identify functional distinct networks according to their temporal independences [41]. Madhyastha et al captured the dynamic change throughout the timecourse by calculating pairwise correlations between nodes in each network in nonoverlapping windows [42]. They also used factor analysis to find the latent structure to explain the functional fluctuating patterns.[42] In

the study of Leonardi et al, principle component analysis (PCA) is used to reveal the hidden patterns of functional connectivity dynamics [43]. Independent component analysis (ICA) is a popular exploratory method for analyzing fMRI experiments. ICA is a 'model-free' method that decomposes the data into different activation patterns [44]. Beckmann et al improved the ICA model by modelling the observations as mixtures of spatially and artefacts in the presence of Gaussian noise. This methodology is called Multivariate Exploratory Linear Optimized Decomposition into Independent Components (MELODIC)[44][45].

Chapter 3 DATA ACQUISITION AND PREPROCESSING

In this section, we will describe the participants and MRI acquisition parameters of our data set as well as the preprocessing pipeline. In our study, we use two data sets, Lexical Retrieval (LR) and Seattle Longitudinal Study (SLS). Participants and MRI acquisition parameters are different for the LR and SLS data sets, so we will describe them in separate paragraphs, but the preprocessing pipelines are the same.

3.1 Participants

There are totally 121 subjects in the SLS data set, 43.8% of which are male and 56.2% of which are female. Their ages range from 56 to 88. They are all cognitively normal. The purpose of the Seattle Longitudinal Study is to study the relationship between aging, health, cognition and lifestyle[46].

There are 19 subjects in the LR data set, 53% of which are male and 47% of which are female. Their ages range from 21 to 53. They are all cognitively normal. The purpose of the study is to investigate which parts of the left temporal lobe support lexical processing stages during picture naming, and specifically to identify brain structures supporting lexical selection and phonological code activation, using well established psycholinguistic effects.

3.2 MRI Acquisition

3.2.1 SLS Data Acquisition

Scanning for the SLS study was performed on a Philips 3.0 T Achieva scanner using an 8-channel head coil. A high resolution MPRAGE was obtained using the following parameters: inversion time (TI)=850ms, turbo-field echo (TFE) factor= 214, repetition time (TR) = 7 milliseconds (ms), echo time (TE) = 3.20 ms, flip angle = 8°, shot interval=3000 ms, acquisition matrix size 224x214, reconstructed matrix size 256x256 (field of view=220x220mm), 160 sagittal slices and a slice thickness of 1 mm.

Functional images were obtained using the following parameters: 43 axial slices, slice thickness 3.5mm, repeat time (TR) 2000 ms, TE= 21ms, acquisition matrix= 64x64, voxel size= 3.50mm isotropic, FOV= 220x220mm, volumes= 225 (7.5min). A B0 field map was acquired immediately after functional imaging. All subjects underwent a resting state scan, for which they were instructed to keep their eyes open and focus on a visual fixation cross. Cardiac and respiratory processes were monitored using the scanner's built-in photoplethysmograph placed on the index finger of the right hand and a pneumatic belt strapped around the upper abdomen. Data were sampled at 50Hz, and files containing cardiac and respiratory waveform data were generated for each scan.

The dMRI scan consisted of a single-shot echo-planar sequence with the following parameters: TR/TE/flip angle: 10.5 s/63 ms/90°, a matrix size of 128 × 128, a FoV of 240 × 240 with a 2 mm slice thickness. Diffusion weighting consisted of 32 non-colinear gradient directions, a non-diffusion weighted b0 map and a b-factor set at 1000 s/mm2.

3.2.2 LR data acquisition

Scanning of the LR study was performed on a Siemens TIM 3.0 T Trio. The TR is 2000 ms, and the TE is 30ms. The acquisition matrix is 64x64, and the FOV is 240 mm. The parameters of dMRI scan are: number of gradient directions is 64, b-factor is 1000s/mm2 and isotropic resolution is 2mm. The scanner is a Siemens Trio 3T scanner.

3.3 MRI Image Preprocessing

3.3.1 Preprocessing of functional MRI data

Functional images of the SLS were processed using software from FSL [47], FreeSurfer [48] and AFNI [49]. Data were corrected for magnetic field inhomogenities using the B0 map, and corrected for motion using FSL MCFLIRT [50]. Mean relative and absolute displacement were calculated for each subject. The resting state pipeline regressed out noise from the cardiac and respiratory signals[51], removed spikes

using AFNI, performed slice timing correction using FSL, and regressed out time series motion parameters and the mean signal for eroded (1mm in 3D) masks of the lateral ventricles and white matter (derived from FreeSurfer). Three dimensional spatial smoothing was performed using a Gaussian kernel with a full width half maximum (FWHM) of sigma=3mm. Data were not normalized as part of the pipeline.

Functional images of LR were motion corrected and unwarped using a B0 field map. The data were smoothed (minimally) with a 1 mm fwhm kernel. This anisotropic smoothing step was performed using SUSAN noise filtering, but with the median smoothing option deselected. The data were highpass filtered to remove frequencies below 100 seconds. The data were filtered to remove motion, cerebrospinal fluid (CSF), and white matter signal confounds by residualizing the data through linear regression. Motion was modeled using the 6 parameter motion correction estimates obtained through motion correction and the temporal derivatives of these motion parameters. CSF and white matter regressors were obtained using the signal time courses from averaging within the eroded CSF mask and an eroded white matter mask, respectively. These tissue masks were constructed from the Freesurfer parcellation of the T1-volume by inverting the transformation from bbregister to map back to the space of the fMRI data. No slice timing correction was performed.

3.3.2 Constructing Tractogram from Diffusion MRI Data

We first removed noise and corrected eddy current distortions using FSL 4.1.8 [47]. We then used BedpostX[4] to estimate diffusion distributions. We then extracted both target ROIs and the seed ROI. The target ROIs are the white matter areas adjacent to 73 major cortical areas in each hemisphere provided by automatic cortical parcellation (2009-Destrieux parcels) [7]. There are 75 major cortical areas in each hemisphere in 2009-Destrieus parcels, but we excluded 2 areas (inferior parietal angular gyrus and inferior parietal supramarginal gyrus) in each hemisphere, because they comprise the IPL. The seed

ROI is the white matter area adjacent to both inferior parietal angular gyrus and inferior parietal supramarmarginal gyrus.

The software we used for automatic cortical parcellation is FreeSurfer, which is documented and freely available for download online (http://surfer.nmr.mgh.harvard.edu/). The technical details of these procedures are described elsewhere ([52];[53];[48];[54];[55];[7];[52][56];[57];[58];[58];[59];[60]). Briefly, this processing includes motion correction and averaging [59] of multiple volumetric T1 weighted images (when more than one is available), removal of non-brain tissue using a hybrid watershed/surface deformation procedure [61], automated Talairach transformation, segmentation of the subcortical white matter and deep gray matter volumetric structures (including hippocampus, amygdala, caudate, putamen, ventricles) ([55]; [57]) intensity normalization [62], tessellation of the gray matter white matter boundary, automated topology correction ([54];[61]), and surface deformation following intensity gradients to optimally place the gray/white and gray/cerebrospinal fluid borders at the location where the greatest shift in intensity defines the transition to the other tissue class ([52];[53];[48]).

We used the FreeSurfer cortical parcellation tool to extract both target ROIs and the seed ROI. Both target and seed ROIs were then nonlinearly registered from FreeSurfer space to diffusion space using FSL registration tools. We eventually performed probabilistic tractography from each seed voxel to each target region for each hemisphere separately using probtrackx[63], a tool of FSL. The final outcome of this step was a two-dimensional connectivity matrix for each hemisphere, in which each row represents the connectivity profile, or tractogram, of a voxel in the seed region with the 73 target regions. The two-dimensional connectivity matrix is also called a tractogram, which provided the basis for dMRI based parcellation.

3.3.3 dMRI Based Parcellation

We first normalized each row of the connectivity matrix by dividing by the largest value of each row of the matrix. Then we computed a connectivity similarity matrix defined by

$$W^{i,j} = exp\left(-d_{Jaccard}(p_i, p_j)\right)$$

in which $W^{i,j}$ is the element of connectivity similarity matrix at the i th row and j th column, $d_{Jaccard}$ is the Jaccard distance (cite) and p_i , p_j are the tractograms of the i th IPL voxel and the j th IPL voxel respectively[19]. $W^{i,j}$ denotes the similarity of the tractogram of the i th IPL voxel and the j th IPL voxel, so each row of the connectivity similarity matrix denotes how similar the tractogram of each IPL voxel is to the tractograms of other IPL voxels. By clustering the rows of the connectivity similarity matrix using the EM algorithm, we parcellated all IPL voxels, thus the dMRI based parcellation was obtained.

3.3.4 Registration of dMRI Based Parcellation to fMRI Space

Because in our study we mainly analyze the dynamics of fMRI signals, dMRI based parcellation of the IPL need to be registered to fMRI space. We first nonlinearly transformed dMRI based parcellation labels from the diffusion space to the FreeSurfer space using FSL registration tool. Then we projected dMRI based parcellation labels from the gray/white matter interface to the surface using FreeSurfer and finally transformed the dMRI based parcellation labels from the surface to the volume of fMRI space using FreeSurfer.

3.3.5 Partial Volume Effect and Its Quantification

The voxel size of fMRI scan is 3mm cubic, however the cortical thickness is usually 2mm, thus an fMRI voxel typically contains a mixture of signals from grey matter, white matter and cerebrospinal fluid (CSF). This is called the partial volume effect. Only signals from grey matter account for real neural activities, so the partial volume effect causes all fMRI voxels to be contaminated by non-neural signals with varying degrees.

We used FAST, a function of FSL to segment the T1 structural image into 3 parts, grey matter, white matter and CSF and then we linearly transformed the maps of grey matter, white matter and CSF from T1 space to fMRI space, respectively, using FLS registration tool. For each voxel of fMRI image, we calculated the percentage of grey matter, white matter and CSF based on the transformed maps of grey matter, white matter and CSF. We used the percentage of grey matter to quantify the degree of partial volume for each voxel.

Chapter 4 DMRI and FMRI-BASED CLUSTERING

In this section, we describe the methods of IPL clustering based on dMRI and fMRI data. The basic idea of IPL voxel clustering is to group voxels that have similar functional or structural connectivity patterns. The dMRI-based clustering method was developed by Soran et al[19].

4.1 dMRI-Based Clustering

The outcome of probabilistic tractography analysis is a connectivity matrix, which contains the probability of a particle moving from each voxel to each target ROI. Such probability is the estimation of the magnitude of structural connection between each voxel and each target ROI. Let C be a connectivity matrix obtained from probabilistic tractography and $C_{i,j}$ be the connectivity between i th voxel and j th target ROI.

We define a metric called tractogram distance indicating the difference between the tractograms of two IPL voxels. Let $tractogram\_dist(i,j)$ be the tractogram distance between the tractogram of voxel i and voxel j. The distance measure we use is the Jaccard metric.

$$tractogram\_dist(i,j) = 1 - \frac{\#\left[(C_{i,t} = C_{j,t}) \cap \left((C_{i,t} \neq 0) \cup (C_{j,t} \neq 0)\right)\right]}{\#\left[(C_{i,t} \neq 0) \cup (C_{j,t} \neq 0)\right]}$$

Then we compute the connectivity similarity matrix W_{conn}

$$W_{conn}^{i,j} = exp(-\alpha * tractogram\_dist(i,j)/\sigma_{conn}^2)$$

$W_{conn}^{i,j}$ indicates the similarity of the tractograms of voxel i and voxel j. $W_{conn}^{i,j}$ is large if the tractograms of voxel i and voxel j are close to each other. Similarly we compute the spatial affinity matrix $W_{spatial}$ defined by

$$W_{spatial}^{i,j} = exp(-(1-\alpha) * dist(i,j)/\sigma_{spatial}^2$$

$W_{spatial}^{i,j}$ indicates the similarity of the geometrical coordinates of voxel i and voxel j. $W_{spatial}^{i,j}$ is large if the geometrical coordinates of voxel i and voxel j are close to each other. Finally we compute the composite similarity matrix $W_{similarity}$

$$W_{similarity}^{i,j} = W_{conn}^{i,j} + W_{spatial}^{i,j}$$

After the construction of the composite similarity matrix, we use the normalized graph-cuts algorithm to cluster the IPL voxels to 7 groups[18]. The number 7 was chosen, because it is the number of regions found in the Jüliech atlas for the IPL area.

4.2 fMRI Based Clustering

The fMRI-based clustering is the clustering of IPL voxels based on the correlation of their functional signals. Voxels whose signals are closely correlated are likely to be in the same cluster. We compute a correlation similarity matrix W_{corr} in which $W_{corr}^{i,j}$is the Pearson correlation between the signals of voxel i and voxel j. Then we cluster the IPL voxels based on the correlation similarity matrix W_{corr} using the EM algorithm[17].

4.3 Evaluating Clustering-Based Parcellations

To validate the dMRI based parcellation, we investigated the following questions: (1) Will subject-specific dMRI parcellations partition fMRI data better than the cytoarchitectonic parcellation estimated from the group-averaged Jüliech atlas, and (2) To what extent are spatial properties of parcellations obtained from dMRI and the Jüliech atlas similar to those obtained from fMRI alone.

4.3.1 Creation of the Subject-Specific Atlas-Based IPL Mask

The reference atlas that we used is the Jüliech Atlas, which is created by averaging 10 post-mortem cyto- and myelo-architectonic segmentations [[11]. This results in a probabilistic map of the IPL. We obtained a unique label for each voxel by assigning to it the parcel with the highest probability (generating a "maximum probability map"). The linear registration from subject T1 space to standard space was used to transform the atlas into subject-specific T1 space, creating an atlas-based IPL-mask. However, this approach suffers from some inaccuracies, and does not correspond to the method used to obtain the DMRI-based mask. To obtain a more accurate map for each individual, we used FreeSurfer [6] to obtain a surface-based mask of the IPL based on anatomical landmarks. The labels for the parcels that make up the IPL are: G_pariet_inf-Angular, G_pariet_inf-Supramar and S_interm_prim-Jensen. We expanded the labels from the surface into the grey matter to obtain a cortical mask. Finally, to derive an atlas-based parcellation of this cortical mask, we intersected the cortical mask with the atlas-based IPL mask, keeping only voxels that appeared in both, and assigned labels to these remaining voxels as in the atlas-based IPL mask. This generated a subject-specific atlas-based IPL mask.

4.3.2 Evaluation of Parcellation

Our intuition for the evaluation of the parcellation is as follows. We assume that function follows structure, and that each region of the IPL that is cytoarchitecturally distinct is more closely connected to some regions of the brain than are other regions of the IPL. Therefore, the fMRI signal within each region of the IPL should be more similar to itself than to other regions of the IPL. The parcellation obtained from dMRI-based connectivity should be more accurate for an individual than the parcellation obtained by merely coregistering the atlas to the subject, because there is a lot of variability in the cortical patterns from one person to the next. However, there is no ground truth by which to judge the dMRI-based parcellation, because accurate cytoarchitectural measurements of the type used to produce the atlas cannot be made on living individuals. Thus, a validation of sorts of the DMRI-based parcellation can be obtained by comparing the dMRI-based parcellation to the atlas-based parcellation on metrics to assess the quality of clustering. The metrics that we used are as follows:

(1) Spatial coherence: The average of spatial deviation (the standard deviation of the coordinates of each cluster). The bigger the spatial coherence is, the worse the clustering quality is.

(2) SIL (Silhouette) metric: [64] This metric is based on computing the average distance of the point to members of the other clusters with the average distance of a point to members of its own cluster. A point is well clustered if it is closer on average to members of its own cluster than to points of other clusters. The SIL statistic is the average of the point silhouettes. The bigger the SIL value, the better the clustering quality.

(3) Davies Bouldin (DB) index:[65] This metric is based on a ratio of two metrics computed for each cluster – one which measures the separation between that cluster and all others (Euclidian distance), and the other which measures the within-cluster scatter (spatial deviation). The bigger the DB index, the worse the clustering quality.

We compared these statistics on the fMRI clusters obtained from a dMRI-based parcellation and the atlas-based parcellation assuming 2-7 clusters existed. The dMRI-based parcellation and atlas originally contain seven clusters. The dMRI-based parcellation results in clusters that are not named, so to determine their correspondence to the atlas-based clustering, we used the Hungarian algorithm [66] to match the dMRI parcels to atlas parcels. However, this matching is far from perfect, and often poor results can occur when successive merges result in discontiguous clusters. To compare smaller numbers of clusters, we successively merged cytoarchitecturally similar clusters according to a hierarchical structure (see Figure 3) defined by receptor architectonics [67] , which matches the cytoarchitectonic parcellation but provides an anatomic similarity measure. We decided to merge clusters at this point rather than to recluster the dMRI so that we could make a fair comparison to the atlas. This assumes that the cytoarchitectural structure represented by the atlas is a "ground truth" that governs function, but that the dMRI-based parcellation is a more accurate representation of the boundaries of the IPL regions. An alternative to merging clusters would be to simply recluster the dMRI data to generate different numbers

of clusters, and to compare against merged regions within the atlas-based parcellation. However, because regional boundaries are likely to change upon reclustering, the results of this approach would have a slightly different interpretation. At the point where the DMRI based clustering better distinguishes functional data than the atlas, one would assume that the DMRI data only supports that number of clusters. Also considering the partial volume effect, only voxels that are at least 50% likely to be gray matter are selected for this analysis.

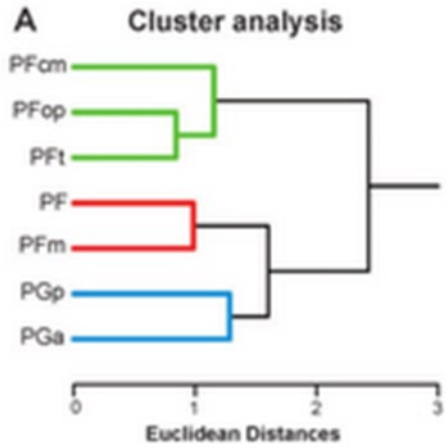

Figure 3 Hierarchical clustering diagram for IPL [67]

4.3.3 Evaluation Results

Table 1 shows evaluations of parcellation results (averaged among 16 subjects). Comparing dMRI parcellation with atlas-based parcellation, it is clear that dMRI-based parcellation better separates the signal in both functional and structural space. At three clusters, dMRI-based parcellation optimally distinguished the functional signal. Comparing structural based (dMRI and atlas) parcellation and fMRI based parcellation, fMRI based clustering methods have larger spatial coherence but better functional clustering quality indicated by DB and SIL index. The quality of the fMRI parcellation and cluster evaluation statistics were significantly influenced by partial volume effects improved by minimal smoothing. The fMRI parcellation showed good spatial overlap with the dMRI parcellation at 3 clusters as shown in Figure 4. These findings are consistent with the idea that fMRI and dMRI may define the same functional anatomical units.

#clusters	2	3	4	5	6	7
dMRI based parcellation						
DB	3.51	1.73	1.83	1.87	2.03	2.01
SIL	0.10	0.16	0.04	-0.06	-0.06	-0.13
Spatial Coherence	5.00	2.62	1.91	1.91	1.91	1.91
Atlas based parcellation						
DB	1.38	1.76	1.85	1.88	1.91	2.06
SIL	0.35	0.11	0.01	-0.01	0.03	-0.04
Spatial Coherence	4.38	2.95	2.26	2.26	2.26	2.26
fMRI based parcellation						
DB	1.05	1.14	1.16	1.20	1.15	1.13
SIL	0.47	0.31	0.25	0.19	0.25	0.29
Spatial Coherence	3.39	3.09	2.93	2.79	2.69	2.56

Table 1 Numerical evaluation of parcellations. Smaller DB value indicates better clustering quality. Bigger SIL values indicate better clustering quality. Smaller spatial coherence indicates better clustering quality.

(A) (B)

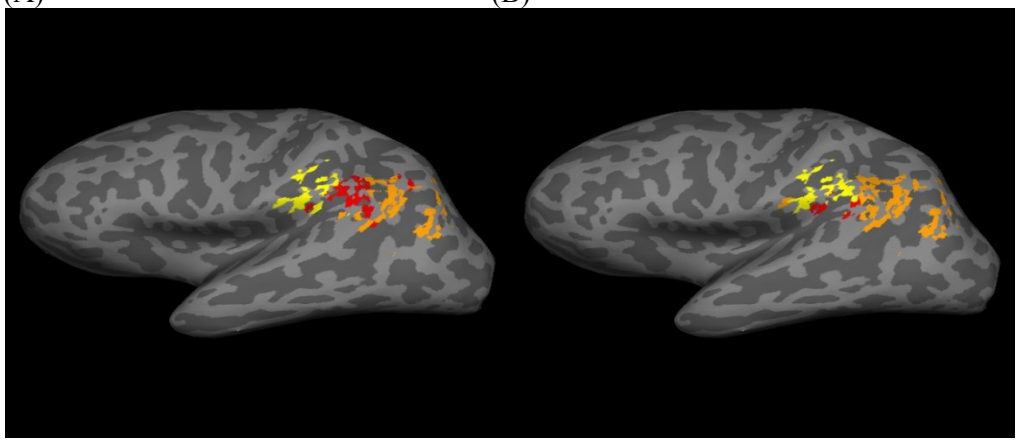

Figure 4 (A) fMRI based parcellation (B) dMRI based parcellation

Chapter 5 DYNAMIC ANALYSIS, MACHINE LEARNING, AND MULTIPLE CLUSTER ANALYSIS

The simple clustering methods of Chapter 4 do not necessarily tell the whole story of the IPL region. In this chapter, we investigate several other methodologies, compare them to the clustering methods, and develop hypotheses about the function of the voxels in the IPL. In section 5.1, we describe methods to differentiate IPL regions using dynamic analysis of resting state functional signals. In section 5.2 and section 5.3, we describe a machine-learning-based parcellation system to parcellate IPL voxels based on the dynamic analysis of resting state functional signals. The system did not work as expected and in section 5.4, we have a thorough analysis of the reasons. From analyzing the reasons of the failed attempt of parcellation, we discovered important patterns of the functional behaviors of individual voxels. In section 5.5, we describe the multiple cluster analysis of IPL voxels and the parcellation of the voxels of different cortical areas based on multiple cluster analysis.

5.1 Dynamic Analysis

As a next step towards parcellation of the IPL, we consider whether the functional connectivity from regions within the IPL and other regions of the brain may provide additional information which would allow us to more finely distinguish cortical fields. Other researchers have taken this approach with results similar to ours [67], resulting in a parcellation of approximately three subregions of the IPL. However, recent work demonstrates that functional connectivity between regions of the brain varies dynamically in time [39]. This suggests the possibility that not only the mean connectivity between regions in the IPL and other regions in the brain, but also the dynamic connectivity, may provide information with which to parcellate the IPL. In this study, we use wavelet transform coherence (WTC) to analyze dynamic connectivity and quantify the connection between different reference ROIs with averaged coherence over time and scale. Because the PGa and PGp cannot be well distinguished using dMRI based parcellation and they are believed to be involved in different networks (i.e., the PGp is more involved in the default

mode network), we hypothesize that the PGa and PGp are connected to the rest of the brain differently in time frequency space. The reference ROIs are 2009-Destrieux parcels [7] provided by Freesurfer.

5.1.1 Wavelet Transform Coherence

Wavelet transform coherence (WTC) is a method for analyzing the coherence and phase lag between two time series as a function of both time and frequency [68]. Intuitively, this analysis finds regions in the time-frequency space where two time series are strongly correlated. We can think of the wavelet coherence as a localized correlation coefficient in time frequency space. This analysis reveals more information than Pearson correlations, traditionally used to examine connectivity, which compare the similarity of the magnitude of signals only in the time domain. The continuous wavelet transform (CWT) is the basis for WTC. Similar to the Short Time Fourier Transform (STFT), CWT was developed to examine the frequency components at given time points, but STFT has a better way of addressing the resolution problem that one can never know precisely what frequency components exist at an exact given time. If a wide window is used for STFT analysis, good frequency resolution and bad time resolution will be achieved and if a narrow window is used, bad frequency resolution and good time resolution will be obtained. In CWT, window size varies with frequency. Bigger windows are used to analyze lower frequency components and smaller windows are used to analyze higher frequency components. Therefore, a reasonable balance between time resolution and frequency resolution will be achieved in CWT. In CWT the signal is convoluted with a wavelet function, similar to the window function in the STFT, and the transform is computed separately for different segments of the time-domain signal[69] .The continuous wavelet transform of a time series x_n of length N, sampled from an underlying continuous waveform at equal time steps of size Δt, is defined as:

$$W^X(n,s) = \sqrt{\frac{\Delta t}{s}} \sum_{n'=1}^{N} x_n \psi_0^* \left[(n'-n) \left(\frac{\Delta t}{s} \right) \right] \qquad (1)$$

where n is a time index and s denotes the wavelet scale. Compared to the Fourier Transform, it is easy to find that the corresponding frequency for scale `s` is `1/s`. Intuitively, high frequencies correspond to the detailed information of a signal that is related to small scale. In this study, the kernel function ψ_0 is chosen to be the complex Morlet wavelet $\psi_0(\eta) = \pi^{-1/4} e^{i\omega_0 \eta} e^{-\eta^2/2}$ and ω_0=6, which has been shown to provide a good trade-off between time and frequency localization. The result of the wavelet transform $W^X(n,s)$ is a complex quantity number. The modulus of $W^X(n,s)$ is the power in time series x with given time and frequency (scale) and the angle represents the local phase.

Similarly, the CWT can be defined for two time series as

$$W^{XY}(n,s) = W^X(n,s)W^{Y*}(n,s) \qquad (2)$$

whose cross-wavelet power $|W^{XY}(n,s)|$ expresses the amount of joint power between X and Y as a function of time and frequency, and whose angle $tan^{-1}(Im\{W^{XY}(n,s)\}/Re\{W^{XY}(n,s)\})$ (cross-wavelet phase) describes their relative phase. Following Torrence and Webster (1999) (cite), the wavelet transform coherence (WTC) is defined as

$$R^2(n,s) = \frac{\left|\langle s^{-1}W^{XY}(n,s)\rangle\right|^2}{\left|\langle s^{-1}W^X(n,s)\rangle\right|^2 \left|\langle s^{-1}W^Y(n,s)\rangle\right|^2} \qquad (3)$$

which reveals localized regions of phase-locked behavior. R^2 ranges between 0 and 1, and can be interpreted as a localized correlation coefficient in time and frequency space [70]. The brackets $\langle\cdot\rangle$ in equation 3 indicate smoothing in both time and scale. Implementation of the WTC and cross-wavelet transform was based on a library of MATLAB functions provided by Grinsted et al [71].

Because wavelet coherence is a statistical measurement affected by the randomness of data, we need to test its statistical significance. To test significance, we first estimate autoregressive (AR) models for the two time series for which wavelet coherence is measured. From the AR models, we generate 300 realizations for each time series, and from calculating the wavelet coherence of each pair of time series

realization we obtain a distribution of possible wavelet coherence values. From the distribution, we calculate the confidence interval of the wavelet coherence value and from which we can declare significance if the wavelet coherence value falls within the confidence interval. This method for significance testing is also implemented in the wavelet toolbox provided by Grinsted et al.

5.1.1.1 Wavelet Coherence Analysis between PGa/PGp and other ROIs

Recalling that the PGa and PGp are parcellated using dMRI as described in Chapter 4, we computed the wavelet coherence between the PGa and PGp and all 107 non-IPL ROIs. We used a probabilistic Jüliech atlas map in which the probability that each voxel belongs to each ROI is listed to probabilistically define the ROIs. Each voxel was assigned to the ROI with the highest probability of containing that voxel. Also if the highest probability is below 40%, that voxel will not be assigned to any ROI. The use of the 0.4 threshold is because according to the study of Eickhoff 2006, the maximal probabilistic map thresholded by 0.4 provides the best representation of the cytoarchitectonic volume [72]. We then calculated the averaged time course within each ROI and performed a wavelet coherence analysis between the time course of the PGa and PGp and the time courses of other ROIs. Results of the WTC analysis of PGa and the left anterior intra-parietal sulcus, an active area within the default mode network, for an example subject are shown in Figure 5.

Areas inside contours with solid lines are areas in which the wavelet coherence value is within a 50% confidence interval. This means that there is a 50% chance that the WTC coherence value of areas within the lines are unlikely to have occurred by chance according to significance test based on bootstrap time courses. Superimposed on this image is a “cone of influence”, outside which confidence values are low due to edge effects, because there are not enough data points outside the cone for reliable WTC calculation.

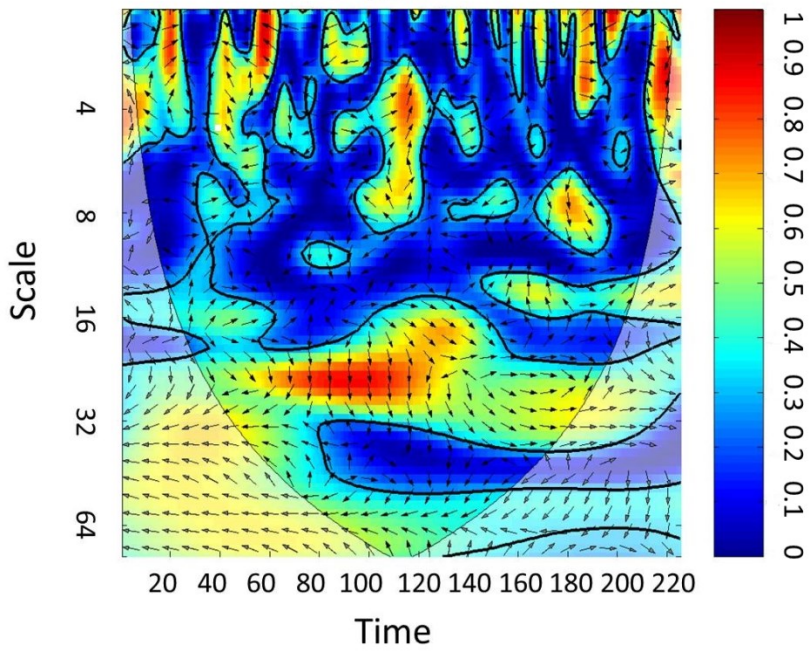

Figure 5 WTC between the PGa and the left anterior intra-parietal sulcus

In the study of Chang et al [39], only areas with above 90% confidence value are considered for further analysis, but instead of 90% as a threshold, we use 50% as the threshold. There is a high degree of noise in the signal, so it will be worse to throw away meaningful information than to keep imprecise values. That is why we use a more liberal threshold here. Only areas with higher than 50% confidence value are considered for any further analysis. The arrow indicates the phase angle between the two time courses at particular time frequency locations. Right pointing arrows indicate positive correlations, while left pointing arrows indicate negative correlations.

5.1.1.2 Scale Averaged Coherence

The result of wavelet coherence analysis between two ROIs is a two-dimensional matrix, but to quantify the connection between two ROIs, we need to reduce the dimensions. Considering that the frequency of resting state oscillations is usually below 0.1 Hz (corresponding to above 10 in scale domain) and in time frequency plot, most points above scale 40 are outside the “cone of influence”, so the average of wavelet

coherence result between 10 and 40 on scale domain should be a good representative of the overall connection between ROIs over time.

We only average wavelet coherence data with above 50% confidence value inside a "cone of influence". Because it is meaningless to average the wavelet coherence magnitudes regardless of the different phases, we average wavelet coherence magnitude with corresponding phase in$[-\pi/4, \pi/4]$, $[\pi/4, 3\pi/4]$,$[3\pi/4, 5\pi/4]$ and$[5\pi/4, 7\pi/4]$ separately.

The formulation of scale averaged coherence between ROI1 and ROI2 for a subject with number *subject#* is given by

$$Scale\_averaged\_coherence(subject\#, ROI1, ROI2, t, \phi) = \frac{1}{N_{coi}(t)} \sum_{s \notin COI(t) and\ 10 \le s \ll 40} R^2(t,s) \cdot I\{R^2(t,s) > a_{50}\} \cdot I\{arg(R^2(t,s)) \in [\phi \pm \pi/4]\} \quad (4)$$

where N_{coi} is the number of pixels outside the cone of influence, a_{50} is the 50% significance level for coherence magnitude, R^2 is defined in Eq(2) and $arg(R^2)$ is the coherence phase. We calculate time averaged coherence and scaled averaged coherence for s$\in [1,64]$, $t \in [1,150]$ and $\phi \in \{0, \pi/2, \pi, -\pi/2\}$. The scale averaged coherence between PGa and the left anterior intra-parietal sulcus is shown in Figure 6.

5.1.1.3 Analysis of Dynamic Networks

In this chapter, we will use the measure of scale averaged coherence introduced in section 5.1.1.2 to quality the different dynamic behaviors of PGa and PGp. First order and second order analysis will be introduced. WTC based method will be compared with a simple statistical method.

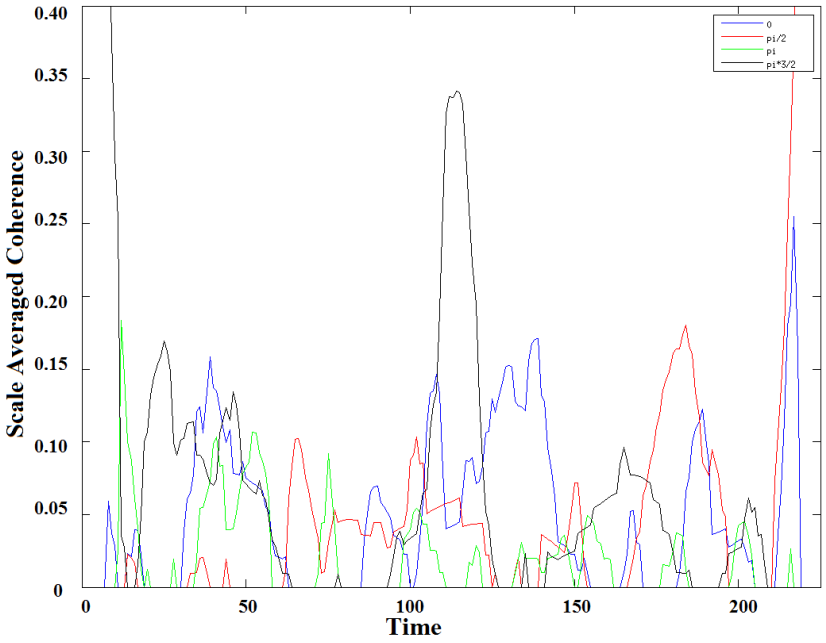

Figure 6 Scale averaged coherence between the PGa and the left anterior intra-parietal sulcus

5.1.1.3.1 First (1st) Order Analysis

As we hypothesized that PGp and PGa interact with the rest of brain with different time-frequency patterns, we expect to see PGa is more strongly functionally connected to some ROIs while the PGp is more strongly functionally connected to some other ROIs. A first-order analysis identifies the individual ROIs that connect to the PGa and PGp with significantly different strength. We compared two ways of measuring the correlation strength. One way is based on scale averaged coherence resulting from wavelet coherence analysis. The other way is the simple Pearson correlation of the time courses.

From the wavelet coherence analysis approach, correlation strength is defined as the mean value of scale averaged coherence over scan time. Intuitively, this is the average coherence within a certain phase angle for all time-frequency points that are significant with a probability of > 50%.The correlation strength between ROI1 and ROI2 for subject# at phase angle ϕ is formulated as

$$corr\_strength(subject\#, ROI1, ROI2, \phi) =$$

$$\frac{1}{duration}\sum_{t=1}^{duration} Scale\_averaged\_coherence(subject\#, ROI1, ROI2, t, \phi) \quad (5)$$

The value of $corr\_strength(subject\#, ROI1, PGa, \phi)$ is the correlation strength between ROI1 and PGa for subject# and the value of $corr\_strength(subject\#, ROI1, PGp, \phi)$ is the correlation strength between ROI1 and PGp for subject#. To test the hypothesis that ROI1 correlates to PGa and PGp with significantly different correlation strength, we performed a paired T-test on the following vector:

[corr_strength(subject1,ROI1,PGa, ϕ),corr_strength(subject1,ROI1,PGp, ϕ)]

[corr_strength(subject2,ROI1,PGa, ϕ),corr_strength(subject2,ROI1,PGp, ϕ)]

[corr_strength(subject3,ROI1,PGa, ϕ),corr_strength(subject3,ROI1,PGp, ϕ)]

…

[corr_strength(subject121,ROI1,PGa, ϕ),corr_strength(subject121,ROI1,PGp, ϕ)]

If the result has over 95% significance, it means the average of the left column vector differs significantly from the right column vector, which further implies that the average correlation strength between the PGa and ROI1 is different from the average correlation strength between the PGp and ROI1.

Repeating the above procedure for all combinations of phase angles ϕ and ROIs, we listed all pairs of phase angle and ROI that show significant PGa/PGp difference in Table 2. There are 30 entries in Table 2 with 20 distinct ROIs.

ROIs	0	π/2	π	3π/2
Grey Matter Anterior intraparietal sulcus hIP1 Left	√		√	
Grey Matter Anterior intraparietal sulcus hIP1 Right	√			
Grey Matter Anterior intraparietal sulcus hIP2 Left	√		√	
Grey Matter Amygdala Centromedial group Right	√			
Grey Matter Broca's area BA44 Right	√		√	
Grey Matter Broca's area BA45 Right	√		√	
Grey Matter Hippocampus cornu ammonis Left	√			
Grey Matter Hippocampus cornu ammonis Right	√	√		
Grey Matter Hippocampus entorhinal cortex Left			√	
Grey Matter Hippocampus dentate gyrus Left	√	√		√
Grey Matter Hippocampus dentate gyrus Right	√	√		√
GM Hippocampus subiculum Left		√		√
GM_Hippocampus_subiculum_R		√		
Grey Matter Primary somatosensory cortex BA1 Left				√
Grey Matter Secondary somatosensory cortex / Parietal operculum OP2 Right			√	
Grey Matter Secondary somatosensory cortex / Parietal operculum OP3 Right	√			
Grey Matter Superior parietal lobule 7M Left	√		√	
Grey Matter Superior parietal lobule 7P Left				√
Grey Matter Premotor cortex BA6 Right				√

Table 2 ROIs and their corresponding phase angle that show significant PGa/PGp difference based on WTC analysis

Then we compared the above results to the simple method in which correlation strength is defined as the Pearson correlation between two ROIs. The ROIs that have significantly different correlations to the PGa and PGp (95% confidence level) are listed in Table 3. There are 18 distinct ROIs.

The comparison shows that there are more significant connections between PGa(PGp) and other ROIs revealed by wavelet coherence analysis than by Pearson correlation analysis, which means there may be more information available for the parcellation of PGa and PGp from the wavelet coherence analysis method.

ROIs
Grey Matter Anterior intraparietal sulcus hIP1 Left
Grey Matter Anterior intraparietal sulcus hIP1 Right
Grey Matter Anterior intraparietal sulcus hIP2 Left
Grey Matter Anterior intraparietal sulcus hIP3 Left
Grey Matter Broca's area BA44 Left
Grey Matter Broca's area BA44 Right
Grey Matter Broca's area BA45 Right
Grey Matter Hippocampus cornu ammonis Left
Grey Matter Hippocampus cornu ammonis Right
Grey Matter Hippocampus entorhinal cortex Left
Grey Matter Hippocampus entorhinal cortex Right
Grey Matter Hippocampus dentate gyrus Left
Grey Matter Hippocampus dentate gyrus Right
GM Hippocampus subiculum Left
Grey Matter Hippocampus subiculum Right
Grey Matter Superior parietal lobule 7M Left
Grey Matter Superior parietal lobule 7M Right

Table 3 ROIs that show significant PGa/PGp difference based on simple method

5.1.1.3.2 Second (2^{nd}) Order Analysis

In the second order analysis, we investigate the correlation between the PGp/PGa and a pair of ROIs instead of a single ROI in time frequency space. We examine how the correlation of the scale averaged coherence defined in Eq(2) between ROI1 and PGa and the scale averaged coherence between ROI2 and PGa differs from the correlation between the scale averaged coherence between ROI2 and PGa and the scale averaged coherence between ROI2 and PGp. We believe the analysis of correlation of correlations will reveal more information of dynamic connectivity than first order analysis.

We give a simple example illustrating how second order analysis works. This example is not based on real data, but is purely by construction. In Table 4 and Table 5, we show the scale averaged coherence plots between PGa (or PGp) and ROIs. Because the mean values of those scale averaged coherences are 0,

all correlation strengths are 0. So from first order analysis, we cannot see any difference between PGa and PGp. However, as shown in the bottom row of the tables, the correlations of two coherence time series are different. This constructed example tells that deeper dynamic connection information can only be revealed by second order analysis, not first order analysis.

	Scale averaged coherence	Correlation Strength
First order analysis of PGa and ROI1	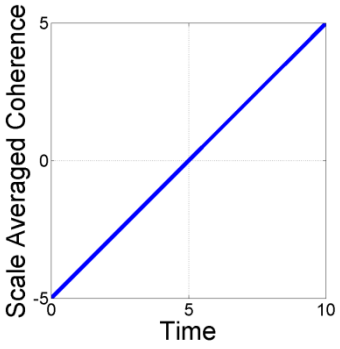	0
First order analysis of PGa and ROI2	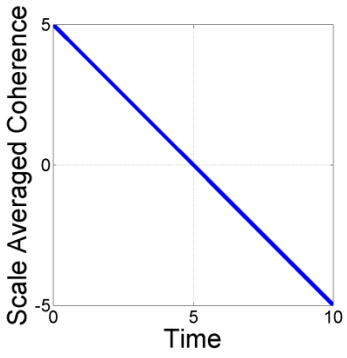	0
Correlation of above two scale averaged coherences	**-1**	

Table 4 Correlation between PGa and a pair of ROIs

	Scale averaged coherence	Correlation Strength
First order analysis of PGa and ROI1	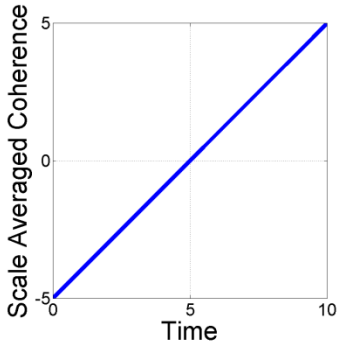	0
First order analysis of PGa and ROI2	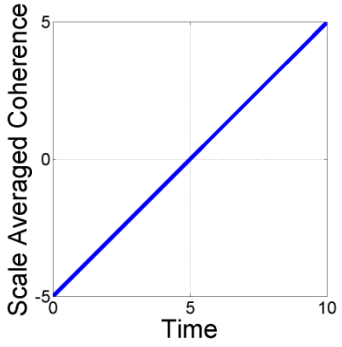	0
Correlation of above two scale averaged coherences	**1**	

Table 5 Correlation between PGp and a pair of ROIs

Here is the formulation for second order analysis. The second order correlation strength between ROI0 and a pair of ROIs (ROI1 and ROI2) for subject# at phase angle ϕ is defined as

$$corr\_strength\_2nd\_order(subject\#, ROI0, ROI1, ROI2, \phi)$$
$$= Pearson\_correlation(Scale\_averaged\_coherence(subject\#, ROI0, ROI1, t, \phi),$$
$$Scale\_averaged\_coherence(subject\#, ROI0, ROI2, t, \phi)) \quad (6)$$

To test the significance of second order correlation strength, we perform a pair T-test on the following vector:

[corr_strength_2nd_order(subject1,PGa,ROI1,ROI2,ϕ),corr_strength_2nd_order(subject1,PGp, ROI1,ROI2,ϕ)]

[corr_strength_2nd_order(subject2,PGa,ROI1,ROI2,ϕ),corr_strength_2nd_order(subject2,PGp, ROI1,ROI2,ϕ)]

…

[corr_strength_2nd_order(subject121,PGa,ROI1,ROI2,ϕ),corr_strength_2nd_order(subject121,PGp, ROI1,ROI2,ϕ)]

If the result has over 95% significance, it means the average of left column vector differ significantly from right column vector, which further implies that the average of the second order correlation strength between PGa and ROI1 and ROI2 is different from the average of the second order correlation strength between PGp and ROI1 and ROI2. Repeating the above procedure for all combinations of phase angles ϕ and ROI pairs, 325 ROI pairs are found to have significant different connection strength with PGa and PGp, and 6 of them are listed in Table 6.

. ROI1	ROI2	0	π/2	π	3π/2
Grey Matter Anterior intraparietal sulcus hIP1 Left	Grey Matter Anterior intraparietal sulcus hIP1 Right			√	
Grey Matter Anterior intraparietal sulcus hIP1 Right	Grey Matter Anterior intraparietal sulcus hIP3 Left		√		
Grey Matter Anterior intraparietal sulcus hIP1 Left	Grey Matter Amygdala laterobasal group Right			√	
…	…				
White Matter Corticospinal tract Right	Grey Matter Insula Ig2 Right				√
White Matter Superior occipito-frontal fascicle Left	Grey Matter Insula Ig2 Right		√		
White Matter Uncinate fascicle Left	Grey Matter Insula Ig2 Right			√	

Table 6 ROI pairs and their corresponding phase angle that show significant PGa/PGp difference based on second order analysis

Then we compare above results from the simple method in which second order correlation strength between ROI0 and a pair of ROIs is defined as the arithmetic difference of the Pearson correlation between ROI0 and ROI1 and the Pearson correlation between ROI0 and ROI2, formulated as

$$corr\_strength\_simple\_method\ (subject\#, ROI0, ROI1, ROI2) = Pearson\_correlation(subject\#, ROI0, ROI1) - Pearson\_correlation(subject\#, ROI0, ROI2) \quad (7)$$

There are 884 ROI pairs found having significant different connection strength with PGa and PGp and 6 of them are listed in the Table 7.

ROI1	ROI2
Grey Matter Anterior intraparietal sulcus hIP1 Left	Grey Matter Anterior intraparietal sulcus hIP1 Right
Grey Matter Anterior intraparietal sulcus hIP1 Left	Grey Matter Anterior intraparietal sulcus hIP3 Left
Grey Matter Anterior intraparietal sulcus hIP1 Left	Grey Matter Anterior intraparietal sulcus hIP3 Right
…	…
GM Hippocampus subiculum Right	Grey Matter Insula Ig2 Right
Grey Matter Superior parietal lobule 7M Left	Grey Matter Insula Ig2 Right
Grey Matter Superior parietal lobule 7M Right	Grey Matter Insula Ig2 Right

Table 7 ROI pairs and their corresponding phase angle that show significant PGa/PGp difference based on simple method

Comparing Table 6 and Table 7, although there are more ROI pairs with significance found by the simple method than wavelet coherence based on second order analysis. Second order analysis does show its power in finding a considerable amount of significant correlations that can be potentially useful for parcellation.

5.1.2 Factor Analysis

Although wavelet coherence analysis provides an effective way of analyzing functional network based on dynamic connectivity, due to the problem of limited resolution, we simply averaged the coherence across time and across scale. Thus the rich information of dynamic connectivity revealed by wavelet method has not been fully explored. Therefore the wavelet-based correlation strength (both 1st order and 2nd order) we

computed still cannot present us the picture of an ‘in-time’ functional network, which reflects the dynamic connectivity of all ROIs.

The reference ROIs selected for analysis are different from the ROIs for wavelet coherence based dynamic functional analysis described in the beginning of section 5.1. In addition to the reference ROIs used in wavelet analysis, we added 3 ROIs (caudate, putamen and hippocampus) that are important subcortical areas of default mode network for each hemisphere. In all subsequent text we refer to this augmented set of ROIs.

Factor analysis is a simple method to quantify dynamic functional networks. We first calculate two aggregated correlation arrays for PGa and PGp respectively. Here are the steps of constructing PGa array and the PGp array is constructed in a similar way. For each subject, we construct a correlation array of PGa. Each row of the correlation array of PGa is the correlations (with z transform) between mean PGa signal and all 154 reference ROIs within a sliding time window of 20TR (40s) long. The sliding window of the `i` th row is between `TR=i` and `TR=i+19`. Because the scan length is 150TR, there are totally 131 sliding windows, hence 131 rows for each subject. We then concatenate the correlation array of each subject vertically to form the aggregated correlation array of PGa. The form of the correlation array of PGa is shown in Table 8. Similarly the correlation array of PGp is constructed (shown in Table 9)

After obtaining the aggregated correlation array of both PGa and PGp, we concatenated them into one array horizontally in which correlations of PGa and correlations of PGp at same time are placed side by side. The form of concatenated aggregated correlation array of PGa and PGp is shown in Table 10. Then we are ready to perform the factor analysis to analyze the joint functional networks of PGa and PGp together. Before applying factor analysis, we need to standardize each row of the concatenated correlation array. Each row is reduced by the row-wise means and then divided by the row-wise standard deviations.

		ROI1	ROI2	…	ROI154
subject1	tw1	corr(tw1,PGa,ROI1)	corr(tw1,PGa,ROI2)		corr(tw1,PGa,ROI154)
	tw2	corr(tw2,PGa,ROI1)	corr(tw2,PGa,ROI2)	…	corr(tw2,PGa,ROI154)
	…	…	…	…	…
	tw130	corr(tw130,PGa,ROI1)	corr(tw130,PGa,ROI2)	…	corr(tw130,PGa,ROI154)
	tw131	corr(tw131,PGa,ROI1)	corr(tw131,PGa,ROI2)	…	corr(tw131,PGa,ROI154)
subject2	tw1	corr(tw1,PGa,ROI1)	corr(tw1,PGa,ROI2)		corr(tw1,PGa,ROI154)
	tw2	corr(tw2,PGa,ROI1)	corr(tw2,PGa,ROI2)	…	corr(tw2,PGa,ROI154)
	…	…	…	…	…
	tw130	corr(tw130,PGa,ROI1)	corr(tw130,PGa,ROI2)	…	corr(tw130,PGa,ROI154)
	tw131	corr(tw131,PGa,ROI1)	corr(tw131,PGa,ROI2)	…	corr(tw131,PGa,ROI154)
…	…	…	…	…	…
subject19	tw1	corr(tw1,PGa,ROI1)	corr(tw1,PGa,ROI2)		corr(tw1,PGa,ROI154)
	tw2	corr(tw2,PGa,ROI1)	corr(tw2,PGa,ROI2)	…	corr(tw2,PGa,ROI154)
	…	…	…	…	…
	tw130	corr(tw130,PGa,ROI1)	corr(tw130,PGa,ROI2)	…	corr(tw130,PGa,ROI154)
	tw131	corr(tw131,PGa,ROI1)	corr(tw131,PGa,ROI2)	…	corr(tw131,PGa,ROI154)

Table 8 Aggregated correlation array of PGa. `tw` refers to time window and `corr` refers to Pearson correlation

		ROI1	ROI2	…	ROI154
subject1	tw1	corr(tw1,PGp,ROI1)	corr(tw1,PGp,ROI2)		corr(tw1,PGp,ROI154)
	tw2	corr(tw2, PGp,ROI1)	corr(tw2,PGp,ROI2)	…	corr(tw2,PGp,ROI154)
	…	…	…	…	…
	tw130	corr(tw130,PGp,ROI1)	corr(tw130,PGp,ROI2)	…	corr(tw130,PGp,ROI154)
	tw131	corr(tw131,PGp,ROI1)	corr(tw131,PGp,ROI2)	…	corr(tw131,PGp,ROI154)
subject2	tw1	corr(tw1,PGp,ROI1)	corr(tw1,PGp,ROI2)		corr(tw1,PGp,ROI154)
	tw2	corr(tw2,PGp,ROI1)	corr(tw2,PGp,ROI2)	…	corr(tw2,PGp,ROI154)
	…	…	…	…	…
	tw130	corr(tw130,PGp,ROI1)	corr(tw130,PGp,ROI2)	…	corr(tw130,PGp,ROI154)
	tw131	corr(tw131,PGp,ROI1)	corr(tw131,PGp,ROI2)	…	corr(tw131,PGp,ROI154)
…	…	…	…	…	…
subject19	tw1	corr(tw1,PGp,ROI1)	corr(tw1,PGp,ROI2)		corr(tw1,PGp,ROI154)
	tw2	corr(tw2,PGp,ROI1)	corr(tw2,PGp,ROI2)	…	corr(tw2,PGp,ROI154)
	…	…	…	…	…
	tw130	corr(tw130,PGp,ROI1)	corr(tw130,PGp,ROI2)	…	corr(tw130,PGp,ROI154)
	tw131	corr(tw131,PGp,ROI1)	corr(tw131,PGp,ROI2)	…	corr(tw131,PGp,ROI154)

Table 9 Aggregated correlation array of PGp. `tw` refers to time window and `corr` refers to Pearson correlation

Aggregated correlation array of PGa	Aggregated correlation array of PGp

Table 10 Concatenated aggregated correlation array of PGa and PGp

Factor analysis is a statistical technique to detect unknown, yet structured patterns that explain the differences in the aggregated correlation arrays. The factor analysis models each measured variable (e.g., the signal at a ROI, or the correlation between two regions) as a linear combination of multiple factor variables plus an error term and an intercept. Let x be a measured variable, w be a common factor variable, e be error of measurement, and τ be an intercept. The factor model is:

$$x_i = \sum \lambda_{ik} w_k + e_i + \tau_i$$

where i denotes the index of the measured variable and k denotes the number of factors [73], [74]. In our analysis, the measured variables are the correlations between the PGa and PGp and all reference ROIs calculated in a time window (40s), so we expect the factors to be 'in-time' functional networks and the loadings of the factor to be the significance of each ROI to the functional network. The number of factors determines the number of dynamic functional networks and the factor loadings indicate how much each ROI contributes to the dynamic network.

While performing factor analysis, we first need to know how many factors (networks) are sufficient to explain the majority of the variation of the measurements. There is no perfect way to determine the "correct" number of factors and for our purposes any reasonable method suffices. A common way to determine the number of factors is the scree analysis [75]. From scree analysis, we selected 7 factors for PGa and PGp. Figure 7 shows the 7 networks of PGa and PGp found by factor analysis side by side. Those networks are in-time networks, which show the simultaneous correlations patterns of PGa and PGp and are compared in Figure 7. Only in the first network (A and H), does PGa have significant different correlation patterns from PGp. In all other networks, PGa and PGp have very similar correlation patterns. This means that in the temporal domain, the difference between PGa and PGp can only be observed once in a while. In section 5.4.1, we will use factor analysis technique to differentiate between the signals of PGa voxels and PGp voxels.

5.2 Machine-learning-based Parcellation for ROIs

From the analysis of the correlation strength (both wavelet-based correlation and simple correlation) between PGa (or PGp) with other reference ROIs described in section 5.1, we see that the correlation strengths between PGa and some reference ROIs are quite different from the correlation strengths between PGp and some reference ROIs. Therefore we expect to use the information of correlation strength to separate the signals of PGa and PGp voxels, which may help refine the parcellation boundary provided by the dMRI method. If this approach turns out to be productive, we would be able to easily extend this method to parcellate other parts of the IPL as well.

Although the differences of PGa and PGp signals shown by previous analysis are statistically significant, it is not easy to formulate such difference in a simple mathematical formula. Instead, we use a machine-learning-based method to differentiate PGa and PGp signals. In our parcellation system, we first train a PGa/PGp classifier based on the feature vectors of some subjects (training set) and then use the classifier to perform PGa/PGp parcellation on the new subjects. The detailed description of the feature vectors are given in section 5.2.1.

Section 5.2 (this section) describes training and testing of the PGp/PGa classification system using the mean signal of PGa and PGp. Therefore, any mention of PGp or PGa signal in this section refers to the mean signal. We will discuss the parcellation of PGa and PGp voxels in section 5.3. It is notable that the mean PGa and PGp signal are calculated from PGa and PGp voxels obtained from the dMRI parcellation. Although the dMRI parcellation is not perfect, it is the best individual parcellation available. The calculation of each mean signal of PGa or PGp might not be very accurate, but a good classifier can still make robust predictions if there are a good number of training instances. Our cross validation results (in section 5.2.3) will show that the classification is not much affected by the inaccuracy of PGa and PGp parcels.

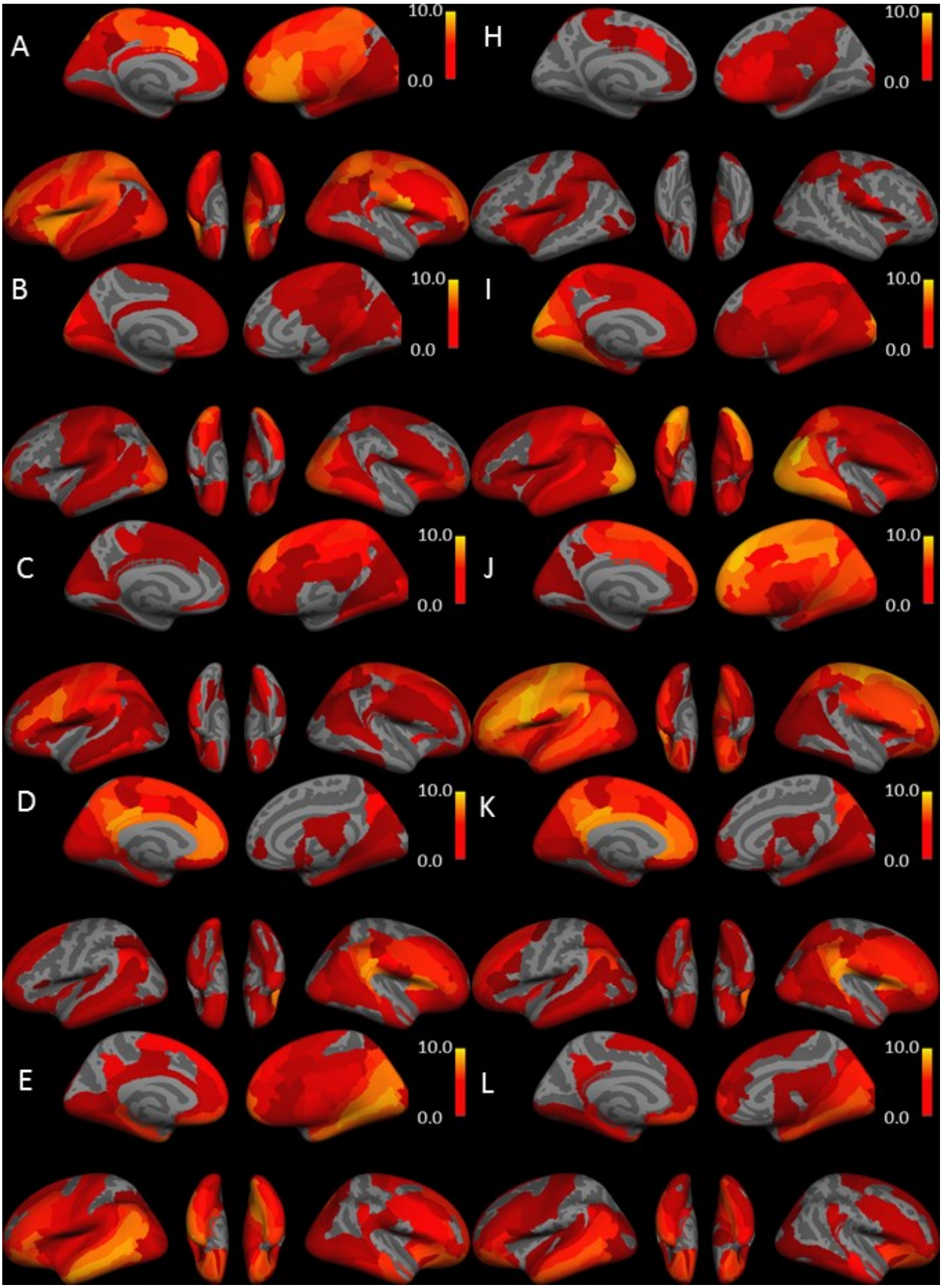
A
10.0
0.0
H
10.0
0.0
B
10.0
0.0
I
10.0
0.0
C
10.0
0.0
J
10.0
0.0
D
10.0
0.0
K
10.0
0.0
E
10.0
0.0
L
10.0
0.0

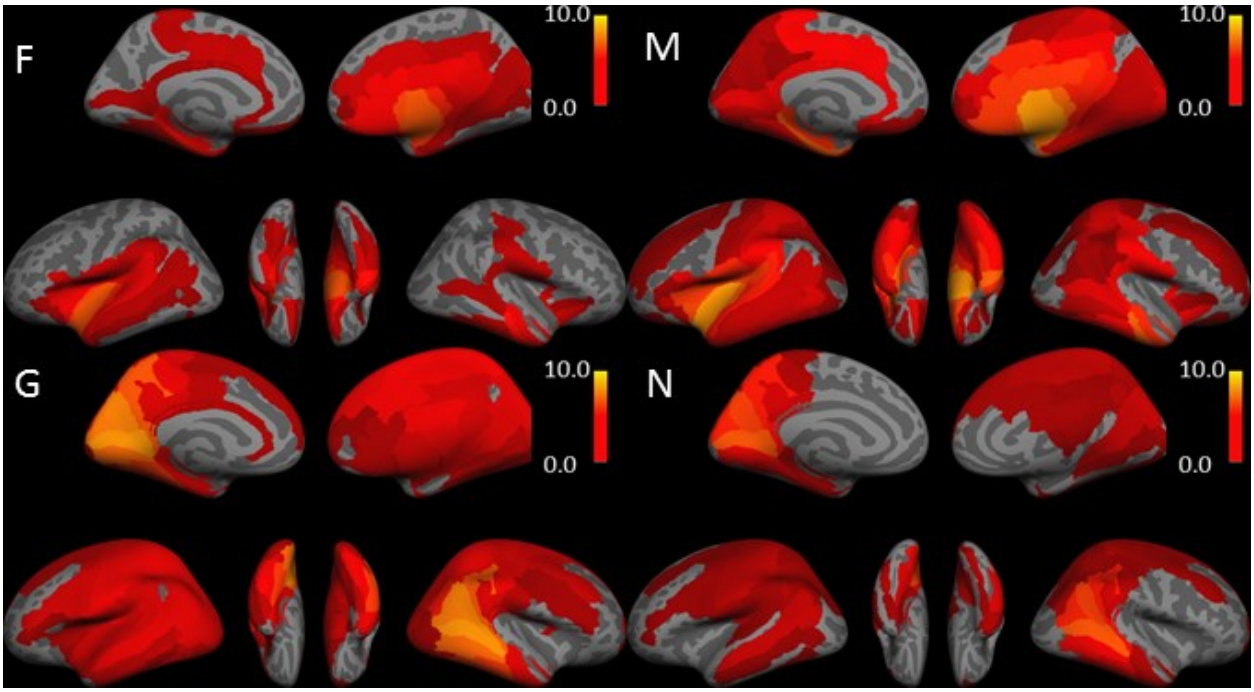

Figure 7 Dynamic functional networks of PGa and PGp. (A), (B), (C), (D), (E), (F) and (G) are the networks of PGa. (H), (I), (J), (K), (L), (M) and (N) are networks of PGp.

5.2.1 The Construction of Feature Vectors

The feature vectors of our classification system are not simply the correlation strength (wavelet-based or simple-correlation-based strength) between the PGa or PGp area of each subject and all the reference ROIs, but instead the correlation strength reduced by the correlation strength of the mean signal of PGa and PGp voxels together. We do this because such subtraction is a way of capturing the unique correlations of the PGa and PGp to other reference ROIs. We call such feature vectors normalized correlation strength. Written in mathematical notation, the normalized correlation strength between PGa and ROI1 is

$$correlation\_strength\_normalized(PGa, ROI1) =$$

$$correlation\_strength(PGa, ROI1) - correlation\_strength(PGa+PGp, ROI1)$$

And the normalized correlation strength between PGp and ROI1 is

correlation_strength_normalized(PGp, ROI1)=

correlation_strength(PGp, ROI1) – correlation_strength(PGa+PGp, ROI1)

To differentiate wavelet-based normalized correlation strength and Pearson-correlation-based normalized correlation strength, we use `wavelet_corr_nd` to notate wavelet-based correlation based normalized correlation strength and `simple_corr_nd` to notate Pearson-correlation-based normalized correlation strength.

We first describe the feature vector construction based on the wavelet method and then describe the feature vector construction based on the simple correlation method.

5.2.1.1 Feature Vectors Based on Wavelet Method

Feature vectors based on the wavelet method are four times as long, because the wavelet correlation strength between PGp or PGa and other reference ROIs is calculated at four phase angles. For each subject, we calculate the wavelet-based normalized correlation strength (`wavelet_corr_nd` in Table 11) between PGa or PGp and all 154 reference ROIs evaluated at all 4 phase angles. As shown in Table 11, there are two feature vectors for each subject: one for PGa and the other for PGp. Concatenating feature vectors of all subjects, we obtain one training feature array shown in Table 11. In our data set, there are 19 subjects, so there are 38 rows in the array. There are 154 reference ROIs and 4 phase angles for the wavelet calculation of each reference ROI, so there are 154*4=616 columns in the array. Thus the size of the feature array is 38 by 616.

	feature1	feature2	…	feature 616	label
subject1	wavelet_corr_nd(subject1,ROI1,PGa,0)	wavelet_corr_nd(subject1,ROI1,PGa,pi/2)	…	wavelet_corr_nd(subject1,ROI154,PGa,3*pi/2)	PGa
	wavelet_corr_nd(subject1,ROI1,PGp,0)	wavelet_corr_nd(subject1,ROI1,PGp,pi/2)	…	wavelet_corr_nd(subject1,ROI154,PGp,3*pi/2)	PGp
subject2	wavelet_corr_nd(subject2,ROI1,PGa,0)	wavelet_corr_nd(subject2,ROI1,PGa,pi/2)	…	wavelet_corr_nd(subject2,ROI154,PGa,3*pi/2)	PGa
	wavelet_corr_nd(subject2,ROI1,PGp,0)	wavelet_corr_nd(subject2,ROI1,PGp,pi/2)	…	wavelet_corr_nd(subject2,ROI154,PGp,3*pi/2)	PGp
	…	…	…	…	…
	…	…	…	…	…
subject19	wavelet_corr_nd(subject19,ROI1,PGa,0)	wavelet_corr_nd(subject19,ROI1,PGa,pi/2)	…	wavelet_corr_nd(subject19,ROI154,PGa,3*pi/2)	PGa
	wavelet_corr_nd(subject19,ROI1,PGp,0)	wavelet_corr_nd(subject19,ROI1,PGp,pi/2)	…	wavelet_corr_nd(subject19,ROI154,PGp,3*pi/2)	PGp

Table 11 Feature vectors of all subjects based on the wavelet method

5.2.1.2 Feature vectors based on simple correlation method

For each subject, we calculated the Pearson correlation (normalized) between the signal of PGa(PGp) and all 154 reference ROIs (notated as simple_corr_nd in Table 12). As shown in Table 12, there are two feature vectors for each subject: one for PGa and the other for PGp. Concatenating feature vectors of all subjects, we obtain one training feature array shown in Table 12. In our data set, there are 19 subjects, so there are 38 rows in the array. There are 154 reference ROIs, so there are 154 columns in the array. Thus the size of the feature array is 38 by 154.

	feature1	feature2	…	feature 154	label
subject1	simple_corr_nd (subject1,ROI1, PGa)	simple_corr_nd (subject1, ROI2,PGa)	…	simple_corr_nd (subject1, ROI154,PGa)	PGa
	simple_corr_nd (subject1,ROI1, PGp)	simple_corr_nd (subject1, ROI2,PGp)	…	simple_corr_nd (subject1, ROI154,PGp)	PGp
subject2	simple_corr_nd (subject2,ROI1, PGa)	simple_corr_nd (subject2, ROI2,PGa)	…	simple_corr_nd (subject2, ROI154,PGa)	PGa
	simple_corr_nd (subject2,ROI1, PGp)	simple_corr_nd (subject2, ROI2,PGp)	…	simple_corr_nd (subject2, ROI154,PGp)	PGp
	…	…	…	…	…
	…	…	…	…	…
subject19	simple_corr_nd (subject19,ROI 1,PGa)	simple_corr_nd (subject19,ROI 2,PGa)	…	simple_corr_nd (subject19,ROI 154,PGa)	PGa
	simple_corr_nd (subject19,ROI 1,PGp)	simple_corr_nd (subject19,ROI 2,PGp)	…	simple_corr_nd (subject19,ROI 154,PGp)	PGp

Table 12 Feature vectors of all subjects based on simple correlation method

5.2.2 The Classification Algorithm

Because we only have 19 training samples, we train a classifier with a simple model to avoid over-fitting. Considering the robustness and simplicity of support vector machine model, we use support vector machine (SVM) with linear kernel to train and test the classification system.

5.2.3 The Cross Validation of the Classification System

We use the 'leave one out' method to cross validate the classification system. To test the parcellation accuracy for each subject, we leave one subject out, train a SVM classifier based on the feature vectors of all remaining subjects, and then apply the trained classifier to predict the label (PGa or PGp) of the feature vectors of the omitted subject. If a PGa feature vector is classified as PGa or a PGp feature vector is classified as PGp, it is considered to be an accurate label prediction, otherwise is not accurate. For each subject, we record the accuracy of classification. We evaluate the performance of the classifier based on the average accuracy of label prediction across subjects. After evaluating the accuracy of the

classification of both wavelet-based features vectors and simple-correlation-based feature vectors, we get 80% accuracy for the wavelet feature vectors and 92.11% for the simple correlation ones. Those numbers indicate considerably high accuracy, which means that the set of feature vectors we use as well as the classification algorithm are highly effective, so we can extend this approach to classify individual IPL voxels.

5.3 Voxel-level Parcellation

As we concluded in Section 5.2, we are able to classify the mean signal of PGa or PGp well using the machine-learning-based parcellation system. In this section, we extend this method to classify individual voxels.

5.3.1 Parcellating the IPL Using Voxel-Level Signals

To parcellate the IPL using voxel-level signals, we use the method described in section 5.2 to train the classifier on mean signals, but the feature vectors of the test subject are different. Instead of using the normalized correlation strength of mean PGa or PGp signal of the test subject as a feature vector, we use the normalized correlation strength of the individual voxels signals of the test subject. Then we use the trained classifier to predict the voxel type (PGa or PGp) of each individual voxel. To evaluate the parcellation, we compare the predictions of each voxel against the dMRI based parcellation and calculate the accuracy (percentage overlap between model predictions and dMRI parcellation). Thus, we are treating the dMRI parcellation as "ground truth" in evaluation of the voxel-based classification method.

To evaluate the overall performance of parcellation over all subjects, we still use the 'leave one out' cross validation approach. For each subject, we train a SVM classifier based on the feature vectors (normalized correlation strength of mean PGa and PGp signals) of all remaining subjects and then apply the classifier to predict the label (PGa or PGp) of each voxel of that subject. After parcellating all subjects, we calculate the average accuracy of the parcellation of each subject to evaluate the overall parcellation performance.

Using this method, we obtained only 53% accuracy for classification based on wavelet features and 57% accuracy for classification based on simple correlation features. These are poor parcellation results. Looking at the parcellation of each subject, we can find many severe misparcellations. The parcellations are shown in Figure 8. Many of parcellations are dominated by one type of voxel (PGa or PGp). Also quite a few parcellations show the randomness of the assignment of PGa and PGp voxels. Only 4 of the 19 parcellations are reasonable and comparable with dMRI based parcellation. Therefore voxel-level parcellation based on above method is a failure. Also wavelet-based feature vectors work even worse than simple-correlation-based feature vectors, although there are more ROIs that have significantly different correlation strength with PGa and with PGp using the wavelet method. Finally, it is much slower to compute wavelet-based features, so we no longer use the wavelet method for later analysis.

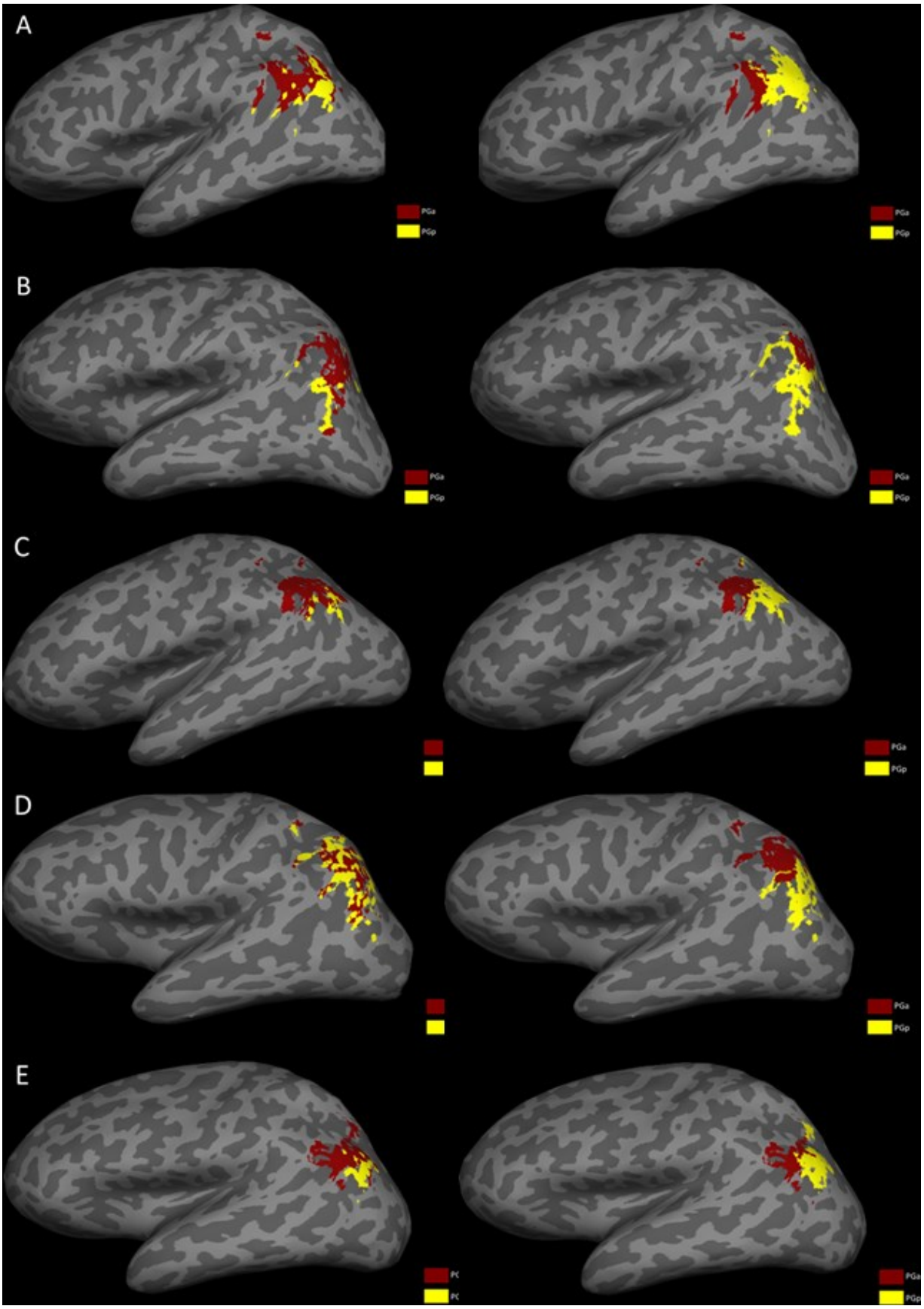
A
PGa
PGp
B
PGa
PGp
C
PGa
PGp
D
PGa
PGp
E
PGa
PGp

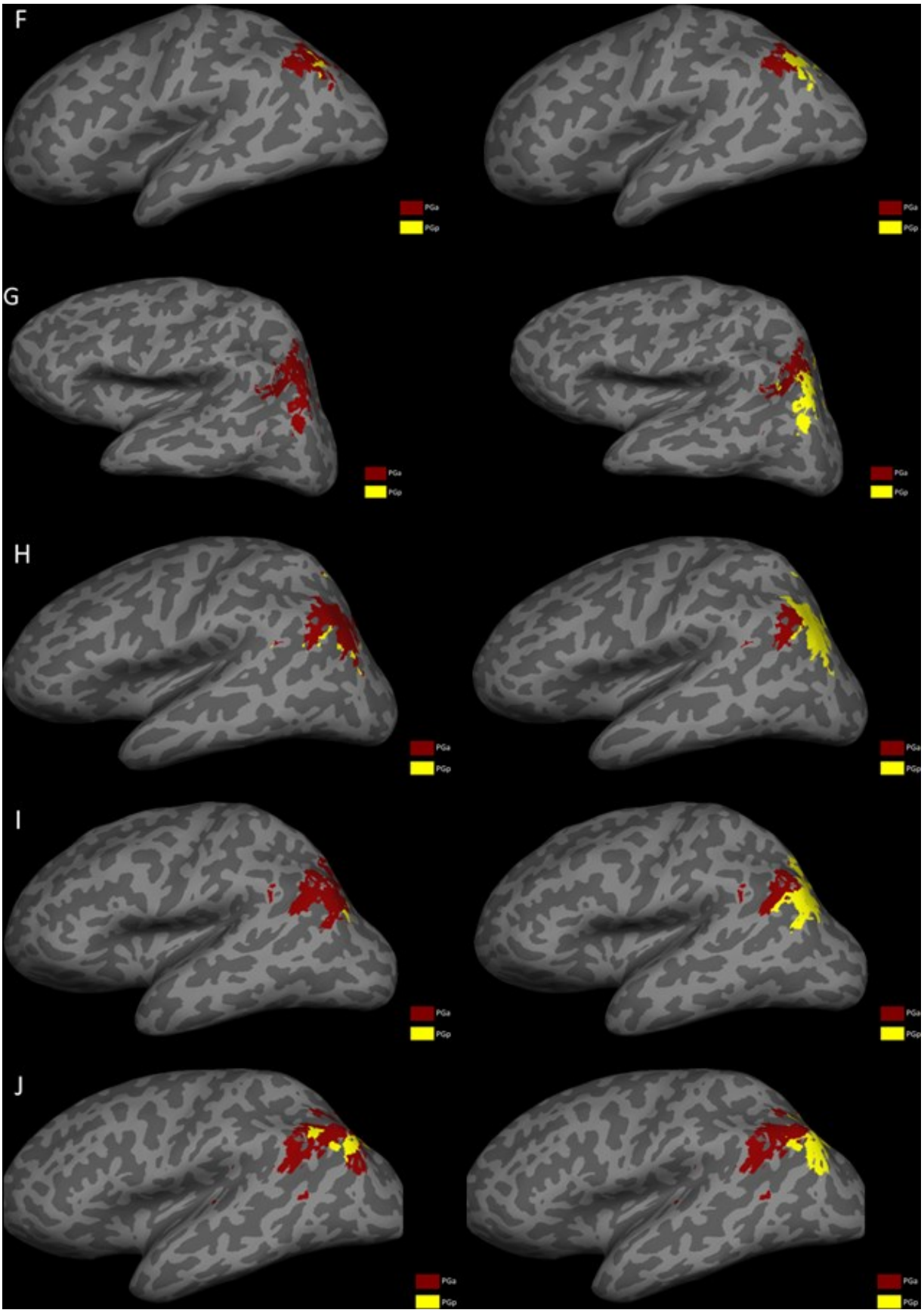
F
PGa
PGp
G
PGa
PGp
H
PGa
PGp
I
PGa
PGp
J
PGa
PGp

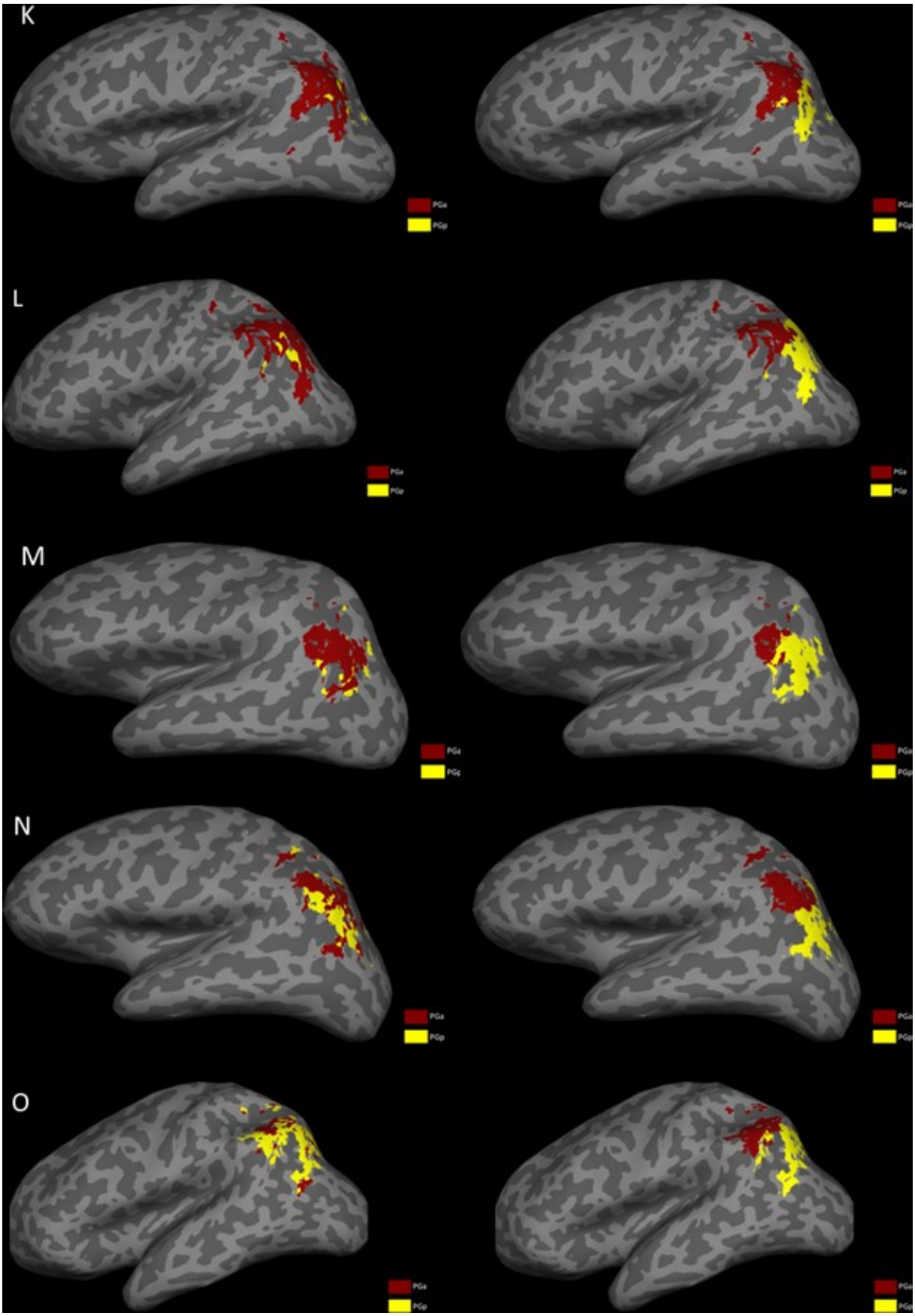
K
PGa
PGp
L
PGa
PGp
M
PGa
PGp
N
PGa
PGp
O
PGa
PGp

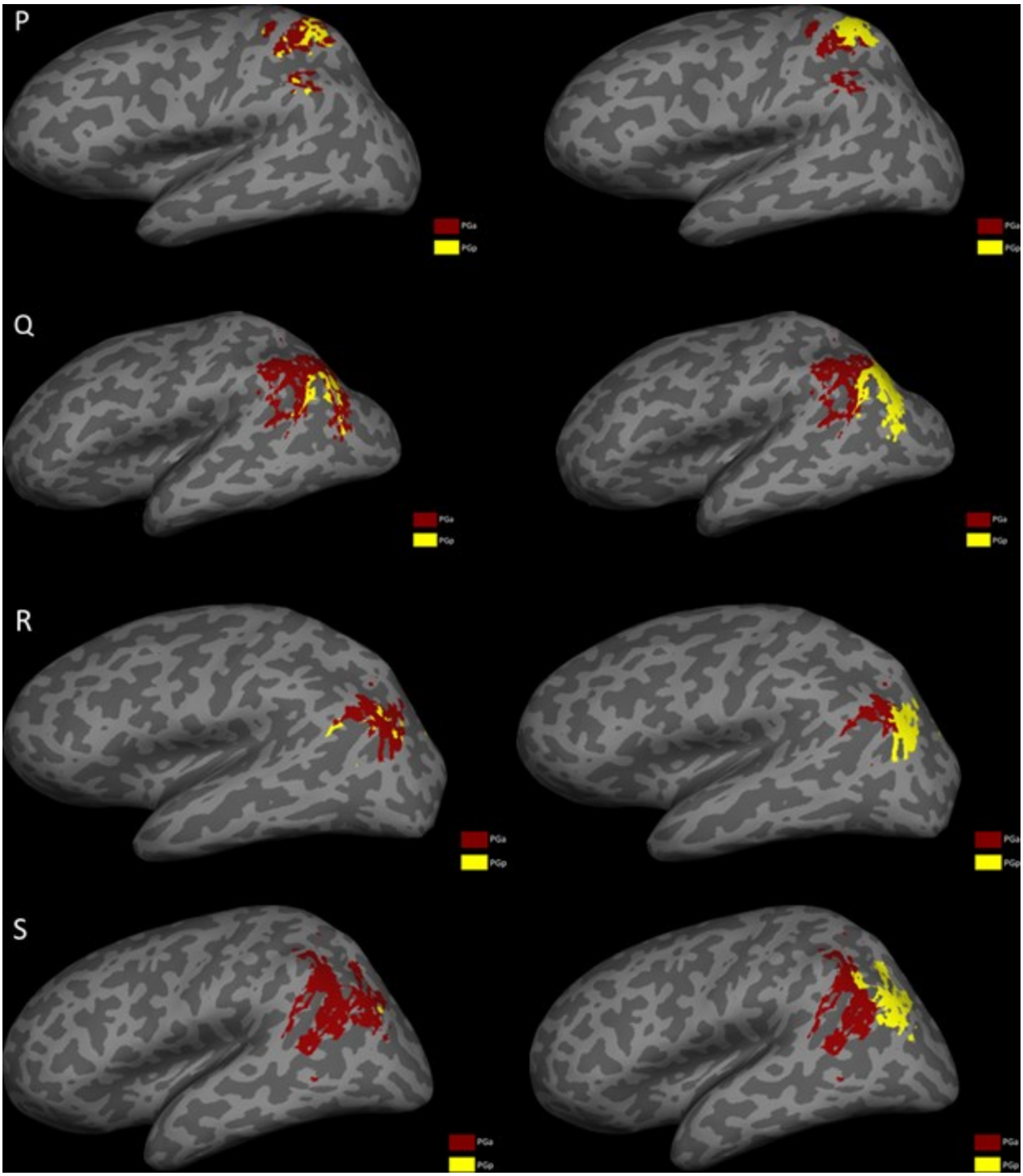

Figure 8 Machine-learning-based functional parcellation of all subjects (on the left) side by side compared with dMRI parcellations (on the right). It is quite obvious that there are no clear boundaries between PGa and PGp voxels in machine-learning-based functional parcellations.

5.4 Investigation of the Unsuccessful Voxel-Based Parcellation

Why was classification of PGp and PGa based on the mean signal so successful, but classification of PGp and PGa voxels using the same methodology failed? To answer this question, we have the following 3 hypotheses.

(1) The lack of the consideration of the dynamic nature of the functional MR signals causes insufficient information to differentiate the signals of PGa and PGp voxels (Section 5.4.1)

(2) The mean signal of PGa or PGp poorly represents individual voxel behaviors, so a fine classification of the mean signal of PGa or PGp cannot guarantee a reasonable classification of individual voxels of PGa or PGp. (Section 5.4.2 and 5.4.3)

(3) Many PGa voxels have PGp-like functional behaviors and vice versa, so many PGa voxels are wrongly classified as PGp and many PGp voxels are wrongly classified as PGa. (Section 5.4.4, 5.4.5 and 5.4.6)

5.4.1 Even factor-analysis-based dynamic analysis cannot provide a reasonable way to separate the different types of voxels

Although wavelet analysis allows quantification of the time-varying relationship of two signals, we collapsed the signal into four average quantities, removing some of the temporal information. Indeed, we found that wavelet analysis did not provide a significantly improved classification over correlation analysis (in section 5.3.1) Therefore, our first suspicion was that the unsuccessful parcellation of voxels in the IPL was attributable to limited information about the dynamic nature of the functional signal. Therefore, we explored whether we were able to distinguish the function of different voxels by using factor analysis of the time-varying signal. The method we used is very similar to the factor analysis method described in section 5.1.2. Instead of analyzing the factors (‘in-time’ functional networks) of mean PGa and PGp signals, we analyze the factors of each voxel as well as the mean signal of PGa and PGp. From the scree test (the method for choosing the number of factors based on the amount of data variance explained), 5 is chosen as the number of the factors of individual voxel. To compare the factor structure of mean PGa and PGp signals and voxels signals conveniently, we choose 5 also as the number

of factors for mean PGa and PGp signals. Then we calculated the congruence between the factor structure of each individual voxel and the factor structure of mean PGa and mean PGp. In factor analysis, a big congruence number indicates close similarity, so in this application, if the factor structure of a voxel has greater congruence with the PGa mean than with the PGp mean, the voxel has more similar 'in-time' functional network structure to mean PGa than mean PGp. Therefore, we determine whether a voxel is functionally PGa or PGp by comparing its congruence with PGa and PGp. Based on this approach, we separate functional PGa voxels and functional PGp voxels for all the subjects.

Figure 9 shows the results side by side compared with structural parcellations. From Figure 9, many PGa voxels functionally behave like PGa and this phenomenon is also observed in the analysis of many other subjects. To quantify this tendency, we calculated the percentage of PGa voxels that are functionally closer to mean PGa, PGa voxels that are functionally closer to mean PGp, PGp voxels that are functionally closer to mean PGa, PGp voxels that are functionally closer to mean PGp for each subject and average them across subjects. Table 13 shows those numbers. From Table 13, it is quite clear that a large number of PGa voxels functionally behave like PGp voxels, and fewer PGp voxels functionally behave like PGa voxels.

(A) (B)

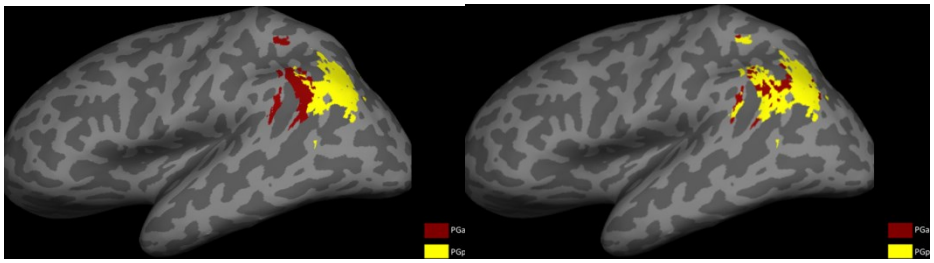

Figure 9 (A) Parcellation based on the factor analysis of voxels' signals (B) Parcellation based on dMRI

	Average percentage across all subjects
'PGa' like PGa voxels	62%
'PGp' like PGa voxels	38%
'PGa' like PGp voxels	28%
'PGp' like PGp voxels	72%

Table 13 The functional behaviors of individual voxels analyzed with factor analysis method. 'PGa' like PGa voxels are PGa voxels that have closer congruency with the factor structure of mean PGa. 'PGp' like PGa voxels are PGa voxels that have closer congruency with the factor structure of mean PGp. 'PGa' like PGp voxels are PGp voxels that have closer congruency with the factor structure of mean PGa. 'PGp' like PGp voxels are PGp voxels that have closer congruency with the factor structure of mean PGp.

Figure 9 and Table 13 clearly suggest that the confusion of PGa and PGp functions is very common. However, we wanted to test our method on regions that are known to have very different functions. Therefore we extend this method to analyze the functional difference between V1 (the vision cortex) and PGp voxels. Because V1 is known to have very little functional correlation with PGp, if the factor-analysis-based approach is sufficient to analyze the differences of voxel-level functional differences, it should at least provide a very reasonable separation of V1 and PGp voxels. The result of applying factor-analysis-based approach to V1 and PGp are shown in Table 14.

	Average percentage across all subjects
'V1' like V1 voxels	69%
'PGp' like V1 voxels	31%
'V1' like PGp voxels	27%
'PGp' like PGp voxels	73%

Table 14 The functional behaviors of individual voxels analyzed with factor analysis method. 'V1' like V1 voxels are V1 voxels that have closer congruency with the factor structure of mean V1. 'PGp' like V1 voxels are V1 voxels that have closer congruency with the factor structure of mean PGp. 'V1' like PGp voxels are PGp voxels that have closer congruency with the factor structure of mean V1. 'PGp' like PGp voxels are PGp voxels that have closer congruency with the factor structure of mean PGp.

However, the results in Table 14 are not what we expected. V1 and PGp voxels signals are not well separated using factor-analysis-based method. The separation between V1 and PGp is only slightly better than the separation between PGa and PGp shown in Table 13. Therefore, we think that even factor-analysis-based dynamic analysis cannot provide a reasonable way to separate different types of voxels. This does not mean that the lack of concern of the dynamic nature of the functional signal is not a reason for previous parcellation failure. This means that only considering the dynamic feature of the signal is insufficient. There should be deeper reasons for unsuccessful voxel-level parcellation.

5.4.2 Correlation of mean signals being higher than voxels signals is caused by the cancellation of high-frequency components with aggregation

The classifier is trained with the correlations of mean PGa and PGp signals, but is used to classify individual voxels signals, so if mean PGa and PGp signals do not well represent individual voxels signals, the classifier is very likely to fail. Here is an example of how we determine whether the mean PGa and PGp signals are really different from individual voxels signals. We calculated the correlation between the mean PGa signal and the mean signal of the ROI dorsal posterior cingulate gyrus as well as the correlation between each of the PGa voxels signals and the mean dorsal posterior cingulate gyrus signal in subject 1. Figure 10 shows all those correlations.

From Figure 10, it is very clear that the correlation between the mean PGa signal and dorsal posterior cingulate gyrus is greater than the correlation between any of the PGa voxels and dorsal posterior cingulate gyrus. Repeating the same calculation for other ROIs and other subjects, we found that in average across subjects, 13.51% of ROIs have greater correlation with mean PGa signal than each individual PGa voxel's signal and 14.90% ROIs have greater correlation with mean PGp signal than each individual PGp voxel's signal. Those results illustrate the hypothesis that the mean PGa and PGp signals do not accurately represent the signals of any individual voxel within those parcels.

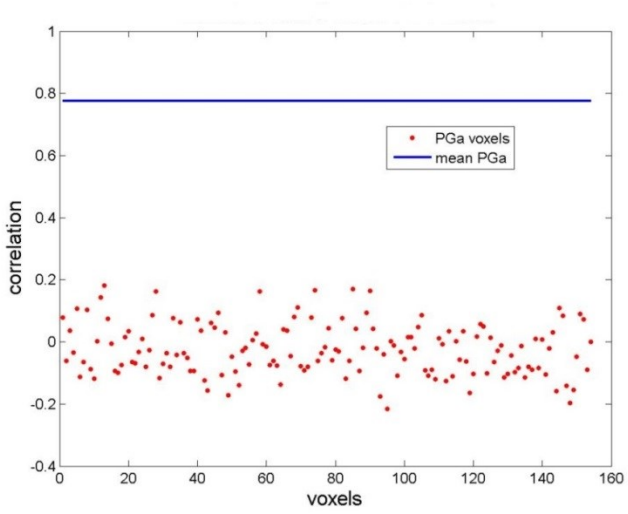

Figure 10 The difference between mean PGa signal and PGa voxels signals in terms of the correlations with the posterior cingulate gyrus.

Because we do not expect the correlation of the average signal to be greater than correlations of all individual signals, we hypothesize that the signal is mixed with some degree of noise in the signal of each voxel. To examine this hypothesis, we did the same correlation analysis on simulated signals of PGa and PGp voxels based on a simple noise generation model. We first simulated the signals of all PGa voxels of subject 3211 based on a simple assumption that the signals of all PGa voxels are the addition of mean PGa voxels signals and a noise term of standard Gaussian distribution (mean is 0 and standard deviation is 1). Here all voxel's signals have all been normalized so that the mean is 0 and standard deviation is 1. Figure 11 shows both real signal and simulated signal of one PGp voxel compared with mean PGa signal. Although it is a very simple noise model, we do see close resemblance of fluctuations between real PGa voxel's signal and the simulated signal of PGa voxel. Then we compared the correlation between the simulated PGa voxels' signals and the signal of dorsal posterior cingulate gyrus as well as real PGa voxels' signals and the signal of dorsal posterior cingulate gyrus, similar to the correlation analysis shown in Figure 10.

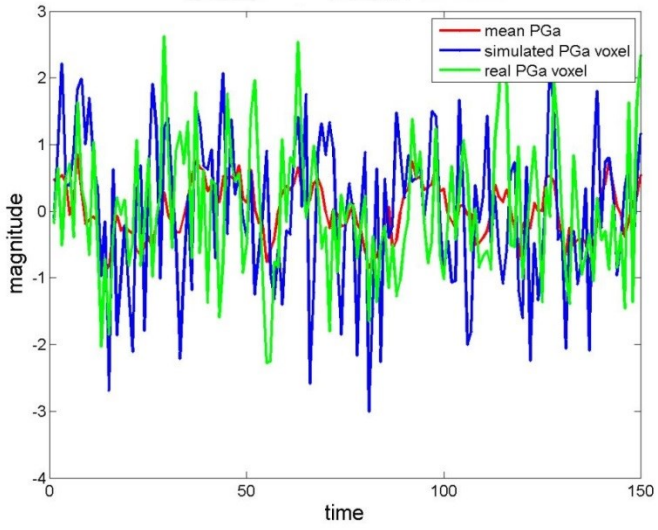

Figure 11 Simulated signal of one PGa voxel

The results are shown in Figure 12. Comparing with Figure 10, the correlations of individual simulated voxels' signal in Figure 12 are generally greater than correlations of the signals of real voxels, which means that the simulated PGa signals do not work in exactly the same way as real PGa voxels. However,

very similar to Figure 10, Figure 12 shows that the correlation of mean simulated PGp signal is also greater than the correlations of any individual simulated voxels' signal. This analysis shows that noise can contribute to the difference between mean ROI signal and individual voxels' signals. Repeating the same analysis with respect to other ROIs gives very similar results.

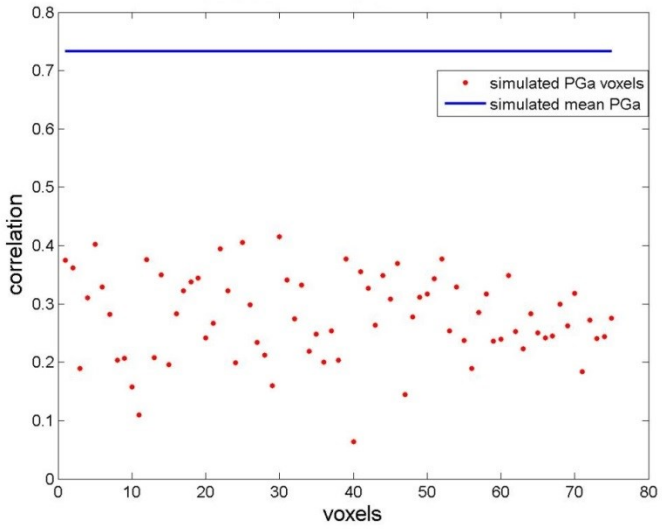

Figure 12 The difference between mean PGa signal and simulated PGa voxels' signals in terms of the correlations with dorsal posterior cingulate gyrus

Based on the correlation analysis of simulated signals, we know that noise is one important reason for the difference between mean signal and voxels signals. In our functional data, we suspect that the high-frequency component of the signal plays a similar role to the noise. Because high-frequency signals cancel each other out when aggregated, the mean signal no longer has a high-frequency part, which causes the difference between the mean signal and individual signals.

5.4.3 Removing high-frequency components does not improve parcellation

To reduce the influence of high-frequency components, we applied a band-pass filter (between 0.01 Hz and 0.1Hz) so that the frequency components above 0.1Hz or below 0.01Hz were filtered out. We found that in average across subjects, only 2.8% ROIs have greater correlation with mean PGa signal than each individual PGa voxel's signal and only 3.5% ROIs have greater correlation with mean PGp signal than

each individual PGp voxel's signal. It is quite obvious that the difference between mean PGa and PGp signal and its voxels signals has been greatly reduced after the filtering of high-frequency components.

Although such difference has been greatly reduced by band-pass filtering, band-pass filtered data does not yield better PGa/PGp parcellation results. The average accuracy of PGa/PGp parcellation is 58% with band pass filtered functional data. This is not surprising because there are theoretical reasons that the high-frequency part of the functional signals should not be simply dismissed. It has been shown that although resting state networks are dominated by the low-frequency part of the functional signal, the high-frequency part of the signal visible within smaller timeframes may contribute to resting state connectivity [76].

5.4.4 Many voxels have a similar correlation to the mean signal of both PGa and PGp

Hypothesis 2 states that many structural PGa voxels have PGp-like functional behaviors and vice versa. To test this hypothesis, we first define that PGa-like voxels are the voxels that have greater correlation with the mean PGa signal than with the mean PGp signal and PGp-like voxels are the voxels that have greater correlation with mean PGp signal than with mean PGp signal. Although mean PGa or PGp signal cannot represent individual PGa or PGp voxels' signal well, correlation with PGa or PGp mean is still the most reasonable way to define 'PGa-like' or 'PGp-like' functional behavior.

In Figure 13, we plot the correlations between voxels' signals and mean PGa and PGp signals in one subject. From Figure 13, it is true that quite a few voxels can be functionally "confused". However after closer look at the "confused" voxels, we are able to see that they are most likely to fall in the middle area (i.e. have close correlation with mean PGa and mean PGp signals). For the voxels that fall in the middle area, they don't exhibit either typical PGa or PGp functional behavior, so the classification of those voxels can be very random, therefore the massive existence of such "middle area" voxels contributes largely to the failure of the previous parcellation system. This observation also violates one of our

previous assumption that all voxels behave either very PGa-like or PGp-like, therefore in order to have a better picture of voxel-level behaviors, there is a need for more sophisticated definition of voxel categorization.

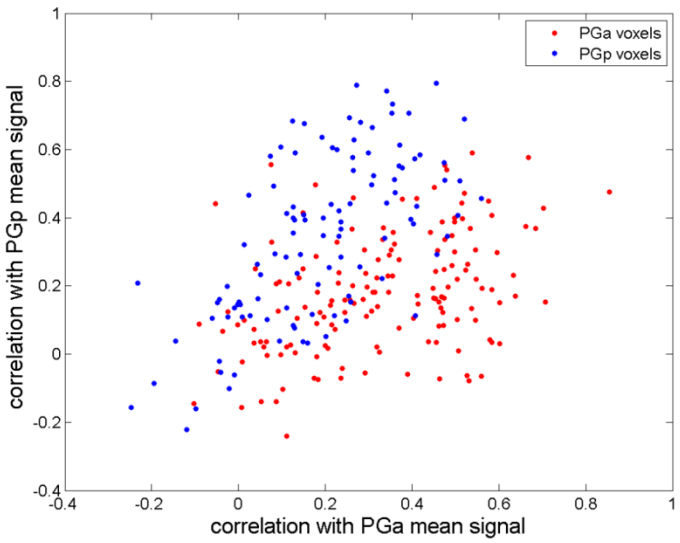

Figure 13 Correlations between voxels' signals and mean PGa/PGp signals

5.4.5 A more comprehensive voxel categorization helps us to understand voxel behavior

In a two ROI system (for example, PGa/PGp or V1/PGp), to better categorize the role of each voxel in terms of its functional correlation with the mean signals of two ROIs, we define five types of voxels: typical voxels, confused voxels, resting voxels, moderate voxels and bridge voxels.

To simplify the notations, let `corr(voxel, ROI1)` be the correlation between the voxel's signal and the mean signal of ROI1 and `corr(voxel, ROI2)` be the correlation between the voxel's signal and the mean signal of ROI2. As shown in Figure 14, the typical voxels of ROI1 are the voxels that satisfy `corr(voxel, ROI1) - corr(voxel, ROI2) >= 0.15`. Conceptually, typical voxels are the voxels that have significant stronger correlation with the ROI1 mean than the ROI2 mean. We used to expect nearly all voxels to be typical voxels. We choose 0.15 as the cutoff value, because nearly half of

the voxels in the PGa/PGp system are categorized as typical voxels if 0.15 is chosen as the cutoff value. Also the 0.15 difference of correlation is big enough, because it is not likely to have resulted from random perturbation. Therefore we consider this is a reasonable way of defining typical voxels. The confused voxels of ROI1 are the voxels that satisfy `corr(voxel, ROI1) – corr(voxel, ROI2) <= -0.15`. It is quite obvious that the confused voxels of ROI1 are the voxels that have significantly stronger correlation with ROI2 mean than ROI1 mean. Those voxels are the ones that we suspect have confused the PGa/PGp classifier.

Voxels other than typical voxels and confused voxels lie in the narrow band between two diagonal lines in Figure 14. They have similar correlation strength with the ROI1 mean and the ROI2 mean. Because they don't exhibit either clearly ROI1-like or clearly ROI2-like, they can be randomly classified as either ROI1 voxel or ROI2 voxel, so we call them ambiguous voxels. The mathematical criteria of ambiguous voxels are voxels that satisfy `abs(corr(voxel, ROI1)- corr(voxel,ROI2)) < 0.15`. Because of the cortical field hypothesis, we do not expect many voxels to fall into the ambiguous category. However, from Figure 14, the simple correlation analysis shows the massive existence of such ambiguous voxels. Therefore we seriously treat them in our voxel categorization system.

We subdivide ambiguous voxels into three classes: resting voxels, moderate voxels and bridge voxels, according to their correlation to both ROIs. The resting voxels are the ambiguous voxels that satisfy `(corr(voxel, ROI1) + corr(voxel, ROI2))/2 <= 0.3`. The moderate voxels are the ambiguous voxels that satisfy `0.3< (corr(voxel, ROI1) + corr(voxel, ROI2))/2 <= 0.5`. The bridge voxels are the ambiguous voxels that satisfy `(corr(voxel, ROI1) + corr(voxel, ROI2))/2 > 0.5`. Conceptually, resting voxels are the voxels that have weak correlations with both ROI1 and ROI2, and it seems that they do not contribute much information to the functional connection between ROI1 and ROI2. Bridge voxels are the voxels that have strong correlation

with both ROI1 and ROI2, and it seems that they serve as a functions bridge between two ROIs. Moderate voxels are the voxels that have moderate functional correlation with both ROI1 and ROI2. In the study of functional brain network analysis, 0.3 is used as a cutoff threshold for weak correlation and 0.5 is used as a cutoff threshold for strong correlation[77], we choose 0.3 as the threshold value between resting voxels and moderate voxels and 0.5 as the threshold value between moderate voxels and bridge voxels.

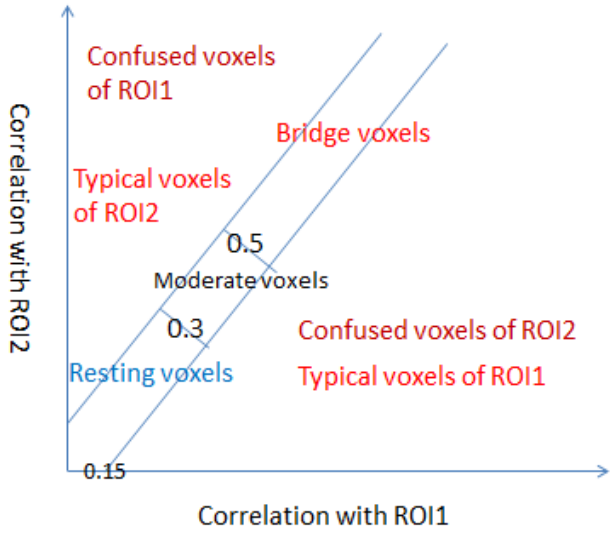

Figure 14 Typical voxels of ROI1 are the voxels that have significant stronger correlation with ROI1 mean than ROI2 mean. Confused voxels of ROI1 are the voxels that have significant stronger correlation with ROI2 mean than ROI1 mean. Similarly confused voxels and typical voxels of ROI2 are defined. Resting voxels are the voxels that have weak correlation with both ROI1 mean and ROI2 mean. Bridge voxels are the voxels that have strong correlation with both ROI1 mean and ROI2 mean. Moderate voxels are the voxels that have neither weak nor strong correlation with both ROI1 mean and ROI2 mean.

5.4.6 Voxel categorization analysis of PGa/PGp and V1/PGp system

We calculated the percentage of each of the five types of voxels in both PGa/PGp system and V1/PGp system. The results are shown in Table 15 and Table 16.

	Mean	SD
Typical voxels	0.33	0.15
Confused voxels	0.02	0.03
Bridge voxels	0.17	0.14
Resting voxels	0.27	0.07
Moderate voxels	0.21	0.05

Table 15 Percentage of each type of voxels in the PGa/PGp system

	Mean	SD
Typical voxels	0.61	0.06
Confused voxels	0.03	0.02
Bridge voxels	0.02	0.03
Resting voxels	0.25	0.05
Moderate voxels	0.08	0.04

Table 16 Percentage of each type of voxels in the V1/PGp system

Comparing the percentage of each type of voxels in the PGa/PGp system and the V1/PGp system, there are much more typical voxels in V1/PGp system than PGa/PGp system. This is expected, because there is strong neurological evidence that PGa and PGp are much stronger connected than V1 and PGp. We also observe that there are a similar number of confused voxels in the PGa/PGp system as in the V1/PGp system, which means that the voxel-level functional confusion between different ROIs rarely takes place in either system. This finding negates our second hypothesis that some structural PGa voxels act functionally more like PGp and vice versa. It is also quite evident that there are many more bridge and moderate voxels in the PGa/PGp system than in the V1/PGp system. This means that it is more common for voxels to work for both PGa and PGp than both V1 and PGp. It is also consistent with the fact that PGa and PGp are much more strongly functionally connected than V1 and PGp. There is also a similar number of resting voxels in the PGa/PGp system and V1/PGp system, which means there are always a number of voxels that correlate weakly to both two ROIs.

Because typical voxels work in the most expected way (i.e. has significantly stronger correlation with the mean signal of its own ROI than the mean signal of other ROI) and resting voxels work in the most unexpected way (i.e. has weak correlation with the mean signal of its own ROI and the mean signal of other ROI). We suspect that there is much less noise in typical voxels than other types of voxels and more noise in resting voxels than other types of voxels. In order to examine the amount of noise in each voxels, we calculated the grey matter percentage for each voxel. The results are shown in Table 17 and Table 18. Because only grey matter contributes to the BOLD signal, we can infer that the more grey matter the voxel contains, the less noise that voxel contains from other physiological sources.

	Mean	SD
Typical voxels	0.49	0.03
Confused voxels	0.45	0.13
Bridge voxels	0.48	0.07
Resting voxels	0.37	0.07
Moderate voxels	0.47	0.05

Table 17 Percentage of grey matter in different types of voxels in PGa/PGp system

	Mean	SD
Typical voxels	0.50	0.02
Confused voxels	0.44	0.12
Bridge voxels	0.46	0.13
Resting voxels	0.38	0.04
Moderate voxels	0.46	0.07

Table 18 Percentage of grey matter in different types of voxels in V1/PGp system

Based on Table 17 and Table 18, we can observe that typical voxels have more grey matter than other types of voxels, while resting voxels have less grey matter than other types of voxels. This relation has been further confirmed by the statistical significance resulted from paired t test across all subjects. Therefore, we can conclude that typical voxels have a more reliable signal and resting voxels contains more amount of noise than other types of voxels. Because resting voxels do not contain a lower percentage of grey matter, it is not surprising that may be contaminated by physiological noise from other sources.

To further examine the role of each type of voxel, we plotted them on the 3D surfaces of the brain of each subject. Figure 15 shows the structural parcellation of PGa and PGp as well as the voxel categorization chart of PGa and PGp. Figure 16 shows the voxel categorization chart of V1and PGp. We can see that in both the PGa/PGp and V1/PGp systems, resting voxels are randomly scattered, reflecting the random nature of noise. In PGa/PGp system, PGa/PGp border voxels are more likely to be bridge voxels than other types of voxels. This can be explained by partial volume effect, because the border voxels are big enough to contain both PGa and PGp neurons, thus the signal can have strong correlation with both PGa and PGp. One important observation is that bridge voxels are not necessarily found on the border. They

can also be found elsewhere. We consider the massive existence of bridge voxels in non-border area as an interesting neurological finding, because this reveals the fact that when two ROIs are strongly correlated, there are areas that correlate simultaneously strongly to both areas. This finding negates the neural activation picture that we anticipated before that all PGa voxels perform in one way uniformly, while all PGp voxels perform in a slightly different way uniformly.

(A) (B)

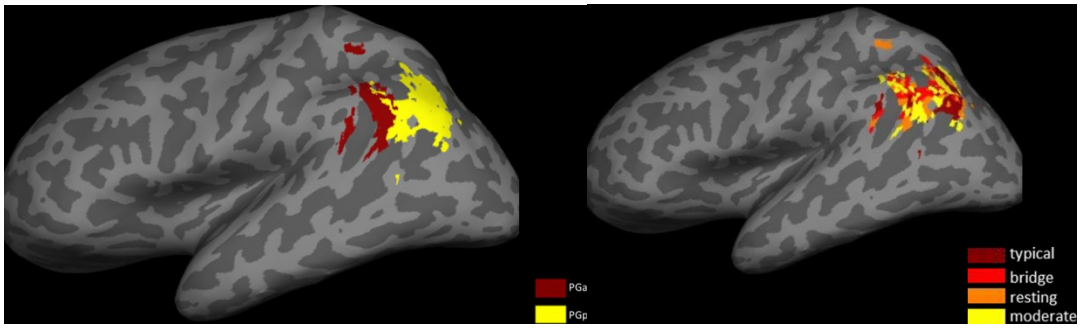

Figure 15 (A) The structural parcellation of PGa and PGp (B) Voxel categorization chart of PGa and PGp

(A) (B)

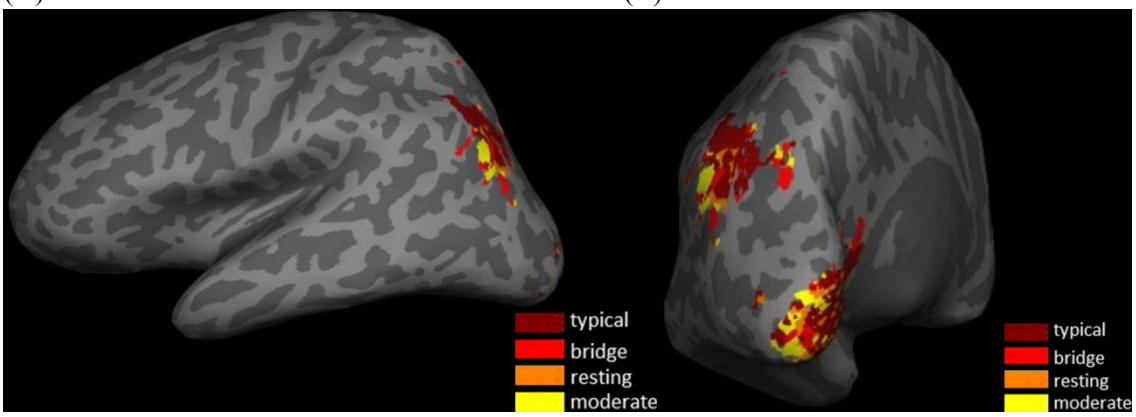

Figure 16 (A) Voxels categorization chart of V1 and PGp (PGp part) (B) Voxels categorization chart of V1 and PGp (V1 part)

5.5 Multiple Cluster Analysis

In section 5.4.6, voxel categorization analysis negates the simple neural activation picture that all voxels in one ROI work in similar function uniformly. Because the functional behaviors of voxels within one ROI cannot explained by a single signal, it is natural to consider the multiple signal model. As described in section 2.3.1, there are many different data clustering algorithms. Because of its simplicity and

effectiveness, we used K-means algorithm to cluster the functional signals within a ROI to find multiple representative signals. We do not mean to imply that K-means is the best clustering algorithm to use here, but because our ultimate purpose here is not clustering, we did not extensively experiment with different clustering algorithms.

5.5.1 K-means Clustering of the Signals

We use the k-means algorithm to find the clusters of the signals of voxels within one ROI. The only input parameter needed for k-means algorithm is the number of clusters. Because our purpose is not to find the optimal clustering of the signals, but a reasonable way to group similar signals, we just use a naïve way to determine the numbers of clusters. For each subject and each ROI, we performed k-means clustering with all possible numbers of clusters (ranging from 1 to number of voxels) and calculated the average within cluster correlation. Figure 17 shows how average within cluster correlation changes over number of clusters for the PGa voxels of one subject. It is quite obvious that average within cluster correlation drops quickly when the number of clusters is small and drops slowly when the number of clusters is large. The turning point is around 8 clusters. After studying such curve for all subjects, we found that the turning points of the average within cluster correlation curve of most subjects are between 5-11 clusters, so we chose 8 as number of clusters for the PGa. Using the same method, we chose 5 as the number of clusters for PGp and 15 as the number of clusters for V1. Figure 18 and Figure 19 shows PGa and PGp clusters clustered by K-means algorithm rendered on brain surface. It is easy to see that the spatial contiguity of each cluster is fairly good; that means the K-means clustering of functional data provides a reasonable partition of the signals within one ROI.

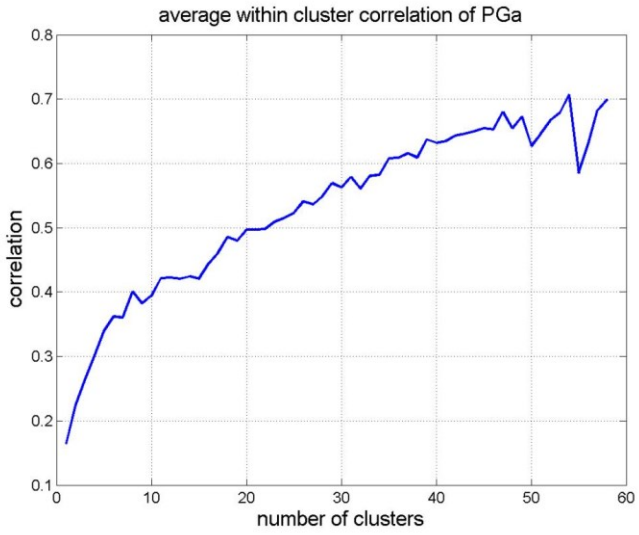

Figure 17 How average within cluster correlation of PGa changes with number of clusters

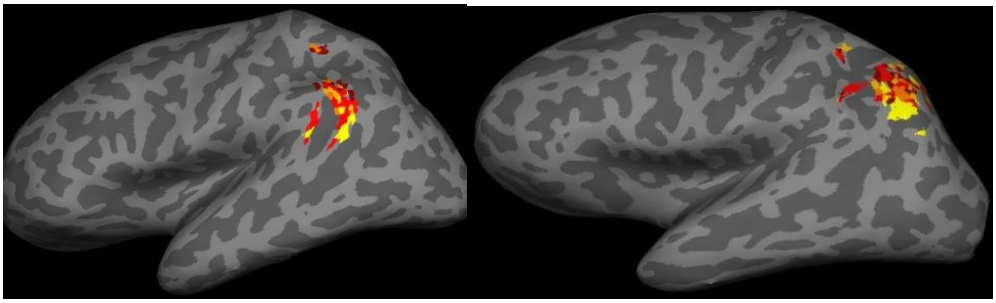

Figure 18 The clustering of PGa voxels of two different subjects(5 clusters)

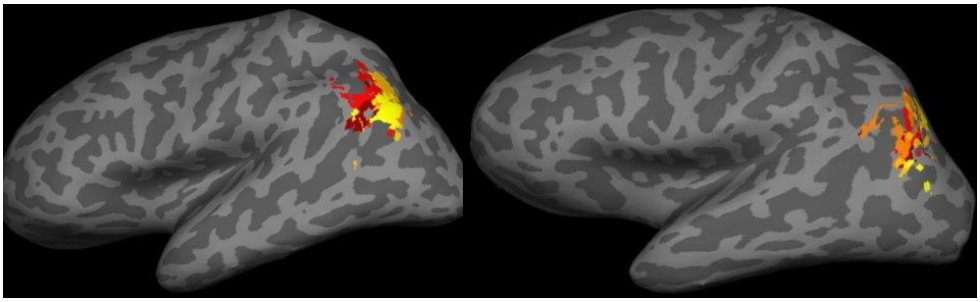

Figure 19 The clustering of PGp voxels of two different subjects (5 clusters)

5.5.2 Multiple-cluster-based Voxel categorization Analysis

To examine whether the multiple cluster model explains individual voxel behaviors better, we first did the voxel categorization analysis. In multiple-cluster-based voxel categorization analysis, the basic concept is still the same as in the voxel categorization analysis described in section 5.4.6, except the correlation between the signal of a voxel and the signal of a ROI need to be redefined. Instead of defining such correlation as the correlation between a voxel's signal and the ROI mean signal, we define it as the maximum correlation between the voxel's signal and the centroid signal of all clusters of ROI. If there is only one cluster in a ROI, the newly defined correlation between that ROI and a voxel is the same as the correlation between that voxel and the ROI mean signal. If there are multiple clusters, the ROI is represented not by its mean signal but by all the cluster centroids, and we call the mean of those clusters 'representatives' of that ROI. The redefined correlation is the closest correlation between those 'representatives' and the voxel.

In multiple-cluster-based voxel categorization analysis, we also calculate the percentage of each five types of voxels as well as the percentage of grey matter in different types of voxels. Table 19 shows the multiple-cluster-based voxel categorization results of PGa/PGp compared with single-cluster-based voxel categorization results. Table 20 shows the multiple-cluster-based voxel categorization results of PGa/PGp compared with single-cluster-based voxel categorization results.

In Table 19 and Table 20, comparing the change of each type of voxels, we notice that there are significantly more typical voxels and bridge voxels and significantly less resting voxels when multiple cluster analysis (based on K-means clustering) is performed. Those changes of numbers had been further confirmed by paired T statistical test. The significant increase of the percentage of typical voxels indicates that multiple cluster analysis differentiates the functional behaviors of PGa/PGp voxels as well as V1/PGp voxels much better than single cluster analysis. Also it is notable that basic conclusions from

multiple-cluster-based voxel categorization analysis still hold here. For example, there are many less typical voxels and many more bridge voxels in PGa/PGp system than in V1/PGp system.

	Single Cluster Analysis		Multiple cluster Analysis	
	Mean	SD	Mean	SD
Typical voxels	0.33	0.15	0.53	0.11
Confused voxels	0.02	0.03	0.01	0.01
Bridge voxels	0.17	0.14	0.30	0.11
Resting voxels	0.27	0.07	0.03	0.02
Moderate voxels	0.21	0.05	0.14	0.06

Table 19 Percentage of each type of voxels in PGa/PGp system

	Single Cluster Analysis		Multiple cluster Analysis	
	Mean	SD	Mean	SD
Typical voxels	0.61	0.06	0.84	0.06
Confused voxels	0.03	0.02	0.00	0.00
Bridge voxels	0.02	0.03	0.08	0.05
Resting voxels	0.25	0.05	0.01	0.01
Moderate voxels	0.08	0.06	0.07	0.02

Table 20 Percentage of each type of voxels in V1/PGp system

5.5.3 Multiple-cluster-based Parcellation

From the multiple-cluster-based voxel categorization analysis, we find that if each ROI is represented by multiple signals, the functional distinction between two types of voxels (either PGa/PGp or V1/PGp) becomes clearer. Inspired by such finding, we expect to improve our machine-learning-based parcellation system by integrating multiple cluster analysis into the parcellation system. In previous parcellation system, each ROI (PGa, PGp or V1) of each subject contributes only one feature vector to the overall training feature set. The feature vector of the ROI is the correlations (normalized) between that ROI and all reference ROIs (ROIs that cover all major areas of the brain). In a multiple-cluster-based parcellation system, each cluster of each ROI of each subject (instead of each ROI of each subject) contributes one feature to the overall training feature set. The feature vector of the cluster is the correlations (normalized) between the centroid of that cluster and all reference ROIs. Because there are multiple cluster for each ROI (5 clusters for PGa and PGp and 15 clusters for V1, the same as in multiple-cluster-based voxel categorization), each ROI of each subject contributes more than one feature vector to the overall training

feature set. Similar to the previous parcellation system, we use a modified cross validation method to test the accuracy of the parcellation system. Each subject is tested by the support vector machine model trained from the training feature vectors collected from all other subjects. The feature vector of the testing subject is the same as in previous parcellation system. After testing all subjects, the average accuracy of voxel type prediction is reported as in section 5.3.

After running the cross validation of multiple-cluster-based parcellation for both PGa/PGp system and V1/PGp system, we got the accuracy report in Table 21. Because PGa and PGp are much more similar to each other to V1 and PGp, it should be easier to parcellate PGa and PGp than V1 and PGp. However the numbers in Table 21 seems to suggest that the parcellation of the PGa/PGp system based on single cluster model is much better than V1/PGP system, which is counter-intuitive. Further analysis shows that nearly all voxels in the V1/PGp system are classified as V1 voxel while voxels in the PGa/PGp system are randomly classified as PGa or PGp with nearly equal chance. Those are equally bad statistical learning outcomes, therefore we consider the parcellations of the PGa/PGp system and V1/PGp system are equally bad.

We see a significant improvement of parcellation accuracy after using multiple-cluster-based parcellation on V1/PGp parcellation and a slight improvement on PGa/PGp parcellation. The improvement of V1/PGp parcellation further confirms that the multiple cluster analysis provides a better way of analyzing voxel behaviors. This means that based on the multiple cluster model, the parcellation of V1 and PGp becomes much easier. It is also not surprising that PGa/PGp parcellation still does not work well, because from Table 21, even using the multiple cluster model, there are still a large number of ambiguous voxels (bridge voxels, moderate voxels and resting voxels) to confuse the training of the features. Because PGa and PGp are spatially adjacent and share many functions, it is not surprising that many voxels work closely with both PGa and PGp and thus the functional boundary between PGa and PGp is rather blurry.

Therefore even based on the multiple cluster model, PGa and PGp voxels still cannot be functionally separated.

	PGa/PGp	V1/PGp
Single-cluster-based parcellation	57%	38%
Multiple-cluster-based parcellation	58%	72%

Table 21 Parcellation accuracy of different parcellation methods

Chapter 6 CONCLUSIONS

In this dissertation, we first validated the dMRI based parcellation of IPL. The results showed that the dMRI based method results in a good three part parcellation, but finer divisions of IPL are not well identified. This indicates the limitation of the exclusive use of structural connectivity information. To overcome this limitation, we examined parcellation methods based on functional connectivity including time frequency analysis. We had shown that PGa and PGp (two adjacent areas of IPL) have significant different connection strength with a set of reference ROIs. We further developed a machine-learning-based parcellation system to differentiate PGa and PGp (also extendable to the parcellation of other ROIs). Although it achieved very good parcellation of the mean signals of PGa and PGp, it did not really provide reasonable parcellations of PGa and PGp voxels. We conducted an in-depth analysis of reasons of the unsuccessful parcellation, including the representation of the time-varying nature of functional data, the difference between the mean ROI signal and ROI voxels signals, and the functional/structural behaviors disparity. During the course of such discussions, we proposed a better metric for categorizing different functional behaviors of different voxels. Eventually we showed that signals of voxels of each ROI cannot be properly represented by any single signal, but the signals are rather formed with multiple cluster. Considering the multiple cluster structure, we did improve the parcellation of V1 and PGp voxels, however, the parcellation of PGa and PGp voxels remained poor. We eventually concluded that the fundamental reason that the signals of PGa and PGp voxels cannot be reasonably clustered is attributed to the massive existence of voxels that co-activate similarly with both PGa and PGp.[78]

Chapter 7 REFERENCES

[1] S. Posse, C. A. Cuenod, and D. Le Bihan, "Human brain: proton diffusion MR spectroscopy," *RADIOLOGY-OAK BROOK IL-*, vol. 188, pp. 719–719, 1993.

[2] P. J. Basser, J. Mattiello, and D. LeBihan, "Estimation of the effective self-diffusion tensor from the NMR spin echo," *J Magn Reson B*, vol. 103, no. 3, pp. 247–254, Mar. 1994.

[3] P. J. Basser and D. K. Jones, "Diffusion-tensor MRI: theory, experimental design and data analysis - a technical review," *NMR Biomed*, vol. 15, no. 7–8, pp. 456–467, Dec. 2002.

[4] T. E. J. Behrens, H. J. Berg, S. Jbabdi, M. F. S. Rushworth, and M. W. Woolrich, "Probabilistic diffusion tractography with multiple fibre orientations: What can we gain?," *Neuroimage*, vol. 34, no. 1, pp. 144–155, Jan. 2007.

[5] C. Destrieux, B. Fischl, A. Dale, and E. Halgren, "Automatic parcellation of human cortical gyri and sulci using standard anatomical nomenclature," *NeuroImage*, vol. 53, no. 1, pp. 1–15, Oct. 2010.

[6] "FreeSurfer." [Online]. Available: http://surfer.nmr.mgh.harvard.edu/. [Accessed: 14-Nov-2012].

[7] B. Fischl, A. van der Kouwe, C. Destrieux, E. Halgren, F. Ségonne, D. H. Salat, E. Busa, L. J. Seidman, J. Goldstein, D. Kennedy, V. Caviness, N. Makris, B. Rosen, and A. M. Dale, "Automatically Parcellating the Human Cerebral Cortex," *Cereb. Cortex*, vol. 14, no. 1, pp. 11–22, Jan. 2004.

[8] J. S. Damoiseaux, S. A. R. B. Rombouts, F. Barkhof, P. Scheltens, C. J. Stam, S. M. Smith, and C. F. Beckmann, "Consistent resting-state networks across healthy subjects," *Proc Natl Acad Sci U S A*, vol. 103, no. 37, pp. 13848–53, Sep. 2006.

[9] M. P. van den Heuvel and H. E. Hulshoff Pol, "Exploring the brain network: a review on resting-state fMRI functional connectivity," *Eur Neuropsychopharmacol*, vol. 20, no. 8, pp. 519–534, Aug. 2010.

[10] R. L. Buckner, J. R. Andrews-Hanna, and D. L. Schacter, "The brain's default network: anatomy, function, and relevance to disease," *Ann. N. Y. Acad. Sci.*, vol. 1124, pp. 1–38, Mar. 2008.

[11] S. Caspers, S. Geyer, A. Schleicher, H. Mohlberg, K. Amunts, and K. Zilles, "The human inferior parietal cortex: Cytoarchitectonic parcellation and interindividual variability," *NeuroImage*, vol. 33, no. 2, pp. 430–448, Nov. 2006.

[12] K. Von Economo and G. Koskinas, "Die Cytoarchitektonik der Hirnrinde des erwachsenen Menschen," *Springer, Wien*, 1925.

[13] L. Q. Uddin, K. Supekar, H. Amin, E. Rykhlevskaia, D. A. Nguyen, M. D. Greicius, and V. Menon, "Dissociable Connectivity within Human Angular Gyrus and Intraparietal Sulcus: Evidence from Functional and Structural Connectivity," *Cereb. Cortex*, vol. 20, no. 11, pp. 2636–2646, Nov. 2010.

[14] R. F. Tungaraza, J. J. Howbert, S. H. Mehta, D. R. Haynor, L. G. Shapiro, and T. J. Grabowski, "Identifying the structural architecture of the human inferior parietal lobule using diffusion MRI," in *2012 9th IEEE International Symposium on Biomedical Imaging (ISBI)*, 2012, pp. 506 –509.

[15] P. e. Roland, S. Geyer, K. Amunts, T. Schormann, A. Schleicher, A. Malikovic, and K. Zilles, "Cytoarchitectural maps of the human brain in standard anatomical space," *Human Brain Mapping*, vol. 5, no. 4, pp. 222–227, 1997.

[16] J. MacQueen, "Some methods for classification and analysis of multivariate observations," presented at the Fifth Berkeley Symposium on Mathematical Statistics and Probability, Statistical Laboratory of the University of California, Berkeley, 1967, vol. 1, pp. 281–297.

[17] A. P. Dempster, N. M. Laird, and D. B. Rubin, "Maximum Likelihood from Incomplete Data via the EM Algorithm," *Journal of the Royal Statistical Society. Series B (Methodological)*, vol. 39, no. 1, pp. 1–38, Jan. 1977.

[18] J. Shi and J. Malik, "Normalized Cuts and Image Segmentation," *IEEE Transactions on Pattern Analysis and Machine Intelligence*, vol. 22, pp. 888–905, 1997.

[19] B. Soran, Z. Xie, R. Tungaraza, S.-I. Lee, L. Shapiro, and T. Grabowski, "Parcellation of Human Inferior Parietal Lobule Based On Diffusion MRI," presented at the EMBC 2012 (34th Annual International Conference of the IEEE Engineering in Medicine and Biology Society), 2012.

[20] D. Davies and D. Bouldin, "A Cluster Separation Measure," *Pattern Analysis and Machine Intelligence, IEEE Transactions on*, vol. PAMI-1, no. 2, pp. 224–227, Apr. 1979.

[21] A. Anwander, M. Tittgemeyer, D. von Cramon, A. D. Friederici, and T. R. Knösche, "Connectivity-Based Parcellation of Broca's Area," *Cereb. Cortex*, vol. 17, no. 4, pp. 816–825, Apr. 2007.

[22] J. C. Klein, T. E. J. Behrens, M. D. Robson, C. E. Mackay, D. J. Higham, and H. Johansen-Berg, "Connectivity-based parcellation of human cortex using diffusion MRI: Establishing reproducibility, validity and observer independence in BA 44/45 and SMA/pre-SMA," *Neuroimage*, vol. 34, no. 1, pp. 204–211, Jan. 2007.

[23] V. Tomassini, S. Jbabdi, J. C. Klein, T. E. J. Behrens, C. Pozzilli, P. M. Matthews, M. F. S. Rushworth, and H. Johansen-Berg, "Diffusion-Weighted Imaging Tractography-Based Parcellation of the Human Lateral Premotor Cortex Identifies Dorsal and Ventral Subregions with Anatomical and Functional Specializations," *J. Neurosci.*, vol. 27, no. 38, pp. 10259–10269, Sep. 2007.

[24] R. B. Mars, S. Jbabdi, J. Sallet, J. X. O'Reilly, P. L. Croxson, E. Olivier, M. P. Noonan, C. Bergmann, A. S. Mitchell, M. G. Baxter, T. E. J. Behrens, H. Johansen-Berg, V. Tomassini, K. L. Miller, and M. F. S. Rushworth, "Diffusion-Weighted Imaging Tractography-Based Parcellation of the Human Parietal Cortex and Comparison with Human and Macaque Resting-State Functional Connectivity," *J. Neurosci.*, vol. 31, no. 11, pp. 4087–4100, Mar. 2011.

[25] H. Huang, J. Zhang, H. Jiang, S. Wakana, L. Poetscher, M. I. Miller, P. C. van Zijl, A. E. Hillis, R. Wytik, and S. Mori, "DTI tractography based parcellation of white matter: Application to the mid-sagittal morphology of corpus callosum," *NeuroImage*, vol. 26, no. 1, pp. 195–205, May 2005.

[26] E. Solano-Castiella, A. Anwander, G. Lohmann, M. Weiss, C. Docherty, S. Geyer, E. Reimer, A. D. Friederici, and R. Turner, "Diffusion tensor imaging segments the human amygdala in vivo," *NeuroImage*, vol. 49, no. 4, pp. 2958–2965, Feb. 2010.

[27] P. Guevara, M. Perrin, P. Cathier, Y. Cointepas, D. Riviere, C. Poupon, and J.-F. Mangin, "Connectivity-based parcellation of the cortical surface using q-ball imaging," in *5th IEEE International Symposium on Biomedical Imaging: From Nano to Macro, 2008. ISBI 2008*, 2008, pp. 903 –906.

[28] M. Beckmann, H. Johansen-Berg, and M. F. S. Rushworth, "Connectivity-Based Parcellation of Human Cingulate Cortex and Its Relation to Functional Specialization," *J. Neurosci.*, vol. 29, no. 4, pp. 1175–1190, Jan. 2009.

[29] J.-H. Kim, J.-M. Lee, H. J. Jo, S. H. Kim, J. H. Lee, S. T. Kim, S. W. Seo, R. W. Cox, D. L. Na, S. I. Kim, and Z. S. Saad, "Defining functional SMA and pre-SMA subregions in human MFC using resting state fMRI: functional connectivity-based parcellation method," *Neuroimage*, vol. 49, no. 3, p. 2375, Feb. 2010.

[30] X. Shen, X. Papademetris, and R. T. Constable, "Graph-theory based parcellation of functional subunits in the brain from resting-state fMRI data," *NeuroImage*, vol. 50, no. 3, pp. 1027–1035, Apr. 2010.

[31] K. Podzebenko, G. F. Egan, and J. D. G. Watson, "Real and Imaginary Rotary Motion Processing: Functional Parcellation of the Human Parietal Lobe Revealed by fMRI," *Journal of Cognitive Neuroscience*, vol. 17, no. 1, pp. 24–36, Jan. 2005.

[32] J. Neumann, D. Y. von Cramon, B. U. Forstmann, S. Zysset, and G. Lohmann, "The parcellation of cortical areas using replicator dynamics in fMRI," *NeuroImage*, vol. 32, no. 1, pp. 208–219, Aug. 2006.

[33] S. Karkar, S. Faisan, L. Thoraval, and J. R. Foucher, "A multi-level parcellation approach for brain functional connectivity analysis," in *Annual International Conference of the IEEE Engineering in Medicine and Biology Society, 2009. EMBC 2009*, 2009, pp. 3497 –3500.

[34] M. G. Woldorff, C. J. Hazlett, H. M. Fichtenholtz, D. H. Weissman, A. M. Dale, and A. W. Song, "Functional Parcellation of Attentional Control Regions of the Brain," *Journal of Cognitive Neuroscience*, vol. 16, no. 1, pp. 149–165, Jan. 2004.
[35] H. Cheng, D. Song, H. Wu, and Y. Fan, "Intrinsic functional connectivity pattern based brain parcellation using normalized cut</title>," 2012, p. 83144F–83144F–9.
[36] A. Tucholka, B. Thirion, M. Perrot, P. Pinel, J.-F. Mangin, and J.-B. Poline, "Probabilistic Anatomo-Functional Parcellation of the Cortex: How Many Regions?," in *Medical Image Computing and Computer-Assisted Intervention – MICCAI 2008*, vol. 5242, D. Metaxas, L. Axel, G. Fichtinger, and G. Székely, Eds. Springer Berlin / Heidelberg, 2008, pp. 399–406.
[37] O. Friman, J. Cedefamn, P. Lundberg, M. Borga, and H. Knutsson, "Detection of neural activity in functional MRI using canonical correlation analysis," *Magnetic Resonance in Medicine*, vol. 45, no. 2, pp. 323–330, 2001.
[38] R. M. Hutchison, T. Womelsdorf, J. S. Gati, S. Everling, and R. S. Menon, "Resting-state networks show dynamic functional connectivity in awake humans and anesthetized macaques," *Human Brain Mapping*, vol. 34, no. 9, pp. 2154–2177, 2013.
[39] C. Chang and G. H. Glover, "Time-frequency dynamics of resting-state brain connectivity measured with fMRI," *Neuroimage*, vol. 50, no. 1, pp. 81–98, Mar. 2010.
[40] D. T. Jones, P. Vemuri, M. C. Murphy, J. L. Gunter, M. L. Senjem, M. M. Machulda, S. A. Przybelski, B. E. Gregg, K. Kantarci, D. S. Knopman, B. F. Boeve, R. C. Petersen, and C. R. Jack, "Non-Stationarity in the 'Resting Brain's' Modular Architecture," *PLoS ONE*, vol. 7, no. 6, p. e39731, Jun. 2012.
[41] S. M. Smith, K. L. Miller, S. Moeller, J. Xu, E. J. Auerbach, M. W. Woolrich, C. F. Beckmann, M. Jenkinson, J. Andersson, M. F. Glasser, D. C. V. Essen, D. A. Feinberg, E. S. Yacoub, and K. Ugurbil, "Temporally-independent functional modes of spontaneous brain activity," *PNAS*, Feb. 2012.
[42] T. M. Madhyastha and T. Grabowski, "Age-Related Differences in the Dynamic Architecture of Intrinsic Networks," *Brain Connectivity*, p. 131213031644004, Dec. 2013.
[43] N. Leonardi, J. Richiardi, M. Gschwind, S. Simioni, J.-M. Annoni, M. Schluep, P. Vuilleumier, and D. Van De Ville, "Principal components of functional connectivity: a new approach to study dynamic brain connectivity during rest," *Neuroimage*, vol. 83, pp. 937–950, Dec. 2013.
[44] S. M. Smith, M. Jenkinson, M. W. Woolrich, C. F. Beckmann, T. E. J. Behrens, H. Johansen-Berg, P. R. Bannister, M. De Luca, I. Drobnjak, D. E. Flitney, R. K. Niazy, J. Saunders, J. Vickers, Y. Zhang, N. De Stefano, J. M. Brady, and P. M. Matthews, "Advances in functional and structural MR image analysis and implementation as FSL," *NeuroImage*, vol. 23, Supplement 1, pp. S208–S219, 2004.
[45] C. F. Beckmann and S. M. Smith, "Probabilistic independent component analysis for functional magnetic resonance imaging," *IEEE Transactions on Medical Imaging*, vol. 23, no. 2, pp. 137–152, 2004.
[46] K. W. Schaie, *Developmental Influences on Adult Intelligence: The Seattle Longitudinal Study*. Oxford University Press, 2012.
[47] M. Jenkinson, C. F. Beckmann, T. E. J. Behrens, M. W. Woolrich, and S. M. Smith, "FSL," *NeuroImage*, vol. 62, no. 2, pp. 782–790, Aug. 2012.
[48] B. Fischl and A. M. Dale, "Measuring the thickness of the human cerebral cortex from magnetic resonance images," *PNAS*, vol. 97, no. 20, pp. 11050–11055, Sep. 2000.
[49] R. W. Cox, "AFNI: Software for Analysis and Visualization of Functional Magnetic Resonance Neuroimages," *Computers and Biomedical Research*, vol. 29, no. 3, pp. 162–173, Jun. 1996.
[50] M. Jenkinson, P. Bannister, M. Brady, and S. Smith, "Improved Optimization for the Robust and Accurate Linear Registration and Motion Correction of Brain Images," *NeuroImage*, vol. 17, no. 2, pp. 825–841, Oct. 2002.

[51] G. H. Glover, T.-Q. Li, and D. Ress, “Image-based method for retrospective correction of physiological motion effects in fMRI: RETROICOR,” *Magnetic Resonance in Medicine*, vol. 44, no. 1, pp. 162–167, 2000.
[52] A. M. Dale, B. Fischl, and M. I. Sereno, “Cortical Surface-Based Analysis: I. Segmentation and Surface Reconstruction,” *NeuroImage*, vol. 9, no. 2, pp. 179–194, Feb. 1999.
[53] A. M. Dale and M. I. Sereno, “Improved Localizadon of Cortical Activity by Combining EEG and MEG with MRI Cortical Surface Reconstruction: A Linear Approach,” *Journal of Cognitive Neuroscience*, vol. 5, no. 2, pp. 162–176, Apr. 1993.
[54] B. Fischl, A. Liu, and A. M. Dale, “Automated manifold surgery: constructing geometrically accurate and topologically correct models of the human cerebral cortex,” *IEEE Transactions on Medical Imaging*, vol. 20, no. 1, pp. 70–80, Jan. 2001.
[55] B. Fischl, D. H. Salat, E. Busa, M. Albert, M. Dieterich, C. Haselgrove, A. van der Kouwe, R. Killiany, D. Kennedy, S. Klaveness, A. Montillo, N. Makris, B. Rosen, and A. M. Dale, “Whole Brain Segmentation: Automated Labeling of Neuroanatomical Structures in the Human Brain,” *Neuron*, vol. 33, no. 3, pp. 341–355, Jan. 2002.
[56] B. Fischl, M. I. Sereno, R. B. Tootell, and A. M. Dale, “High-resolution intersubject averaging and a coordinate system for the cortical surface,” *Human brain mapping*, vol. 8, no. 4, pp. 272–284, 1999.
[57] B. Fischl, A. van der Kouwe, C. Destrieux, E. Halgren, F. Ségonne, D. H. Salat, E. Busa, L. J. Seidman, J. Goldstein, D. Kennedy, V. Caviness, N. Makris, B. Rosen, and A. M. Dale, “Automatically Parcellating the Human,” *Cereb. Cortex*, vol. 14, no. 1, pp. 11–22, Jan. 2004.
[58] X. Han, J. Jovicich, D. Salat, A. van der Kouwe, B. Quinn, S. Czanner, E. Busa, J. Pacheco, M. Albert, R. Killiany, P. Maguire, D. Rosas, N. Makris, A. Dale, B. Dickerson, and B. Fischl, “Reliability of MRI-derived measurements of human cerebral cortical thickness: The effects of field strength, scanner upgrade and manufacturer,” *NeuroImage*, vol. 32, no. 1, pp. 180–194, Aug. 2006.
[59] M. Reuter, H. D. Rosas, and B. Fischl, “Highly accurate inverse consistent registration: A robust approach,” *NeuroImage*, vol. 53, no. 4, pp. 1181–1196, Dec. 2010.
[60] M. Reuter, N. J. Schmansky, H. D. Rosas, and B. Fischl, “Within-subject template estimation for unbiased longitudinal image analysis,” *NeuroImage*, vol. 61, no. 4, pp. 1402–1418, Jul. 2012.
[61] F. Segonne, J. Pacheco, and B. Fischl, “Geometrically Accurate Topology-Correction of Cortical Surfaces Using Nonseparating Loops,” *IEEE Transactions on Medical Imaging*, vol. 26, no. 4, pp. 518–529, Apr. 2007.
[62] J. G. Sled, A. P. Zijdenbos, and A. C. Evans, “A nonparametric method for automatic correction of intensity nonuniformity in MRI data,” *IEEE Transactions on Medical Imaging*, vol. 17, no. 1, pp. 87–97, Feb. 1998.
[63] T. e. j. Behrens, M. w. Woolrich, M. Jenkinson, H. Johansen-Berg, R. g. Nunes, S. Clare, P. m. Matthews, J. m. Brady, and S. m. Smith, “Characterization and propagation of uncertainty in diffusion-weighted MR imaging,” *Magnetic Resonance in Medicine*, vol. 50, no. 5, pp. 1077–1088, 2003.
[64] P. Rousseeuw, “Silhouettes: a graphical aid to the interpretation and validation of cluster analysis,” *J. Comput. Appl. Math.*, vol. 20, no. 1, pp. 53–65, Nov. 1987.
[65] D. L. Davies and D. W. Bouldin, “A Cluster Separation Measure,” *Pattern Analysis and Machine Intelligence, IEEE Transactions on*, vol. PAMI-1, no. 2, pp. 224 –227, Apr. 1979.
[66] H. W. Kuhn, “The Hungarian Method for the Assignment Problem,” in *50 Years of Integer Programming 1958-2008*, M. Jünger, T. M. Liebling, D. Naddef, G. L. Nemhauser, W. R. Pulleyblank, G. Reinelt, G. Rinaldi, and L. A. Wolsey, Eds. Springer Berlin Heidelberg, 2010, pp. 29–47.
[67] S. Caspers, A. Schleicher, M. Bacha-Trams, N. Palomero-Gallagher, K. Amunts, and K. Zilles, “Organization of the Human Inferior Parietal Lobule Based on Receptor Architectonics,” *Cerebral cortex (New York, N.Y.: 1991)*, Feb. 2012.
[68] C. Torrence and G. P. Compo, *A Practical Guide to Wavelet Analysis*. 1998.

[69] “INDEX TO SERIES OF TUTORIALS TO WAVELET TRANSFORM BY ROBI POLIKAR.” [Online]. Available: http://users.rowan.edu/~polikar/WAVELETS/WTtutorial.html. [Accessed: 14-Nov-2012].
[70] A. Grinsted, J. C. Moore, and S. Jevrejeva, “Application of the cross wavelet transform and wavelet coherence to geophysical time series,” *Nonlinear Processes in Geophysics*, vol. 11, no. 5/6, pp. 561–566, Nov. 2004.
[71] “Crosswavelet and Wavelet Coherence.” [Online]. Available: http://www.pol.ac.uk/home/research/waveletcoherence/. [Accessed: 14-Nov-2012].
[72] S. B. Eickhoff, S. Heim, K. Zilles, and K. Amunts, “Testing anatomically specified hypotheses in functional imaging using cytoarchitectonic maps,” *NeuroImage*, vol. 32, no. 2, pp. 570–582, Aug. 2006.
[73] J. L. Horn and J. J. McArdle, “A practical and theoretical guide to measurement invariance in aging research,” *Exp Aging Res*, vol. 18, no. 3–4, pp. 117–144, Autumn-Winter 1992.
[74] W. Meredith and J. A. Teresi, “An essay on measurement and factorial invariance,” *Med Care*, vol. 44, no. 11 Suppl 3, pp. S69–77, Nov. 2006.
[75] R. B. Cattell, “The Scree Test For The Number Of Factors,” *Multivariate Behavioral Research*, vol. 1, no. 2, pp. 245–276, 1966.
[76] R. K. Niazy, J. Xie, K. Miller, C. F. Beckmann, and S. M. Smith, “Spectral characteristics of resting state networks,” *Prog. Brain Res.*, vol. 193, pp. 259–276, 2011.
[77] M. P. van den Heuvel, C. J. Stam, R. S. Kahn, and H. E. H. Pol, “Efficiency of Functional Brain Networks and Intellectual Performance,” *J. Neurosci.*, vol. 29, no. 23, pp. 7619–7624, Jun. 2009.
[78] S. Caspers, S. B. Eickhoff, T. Rick, A. von Kapri, T. Kuhlen, R. Huang, N. J. Shah, and K. Zilles, “Probabilistic fibre tract analysis of cytoarchitectonically defined human inferior parietal lobule areas reveals similarities to macaques,” *NeuroImage*, vol. 58, no. 2, pp. 362–380, Sep. 2011.